Cell Metabolism

Article

Remote limb ischemic conditioning alleviates steatohepatitis via extracellular vesicle-mediated muscle-liver crosstalk

Graphical abstract

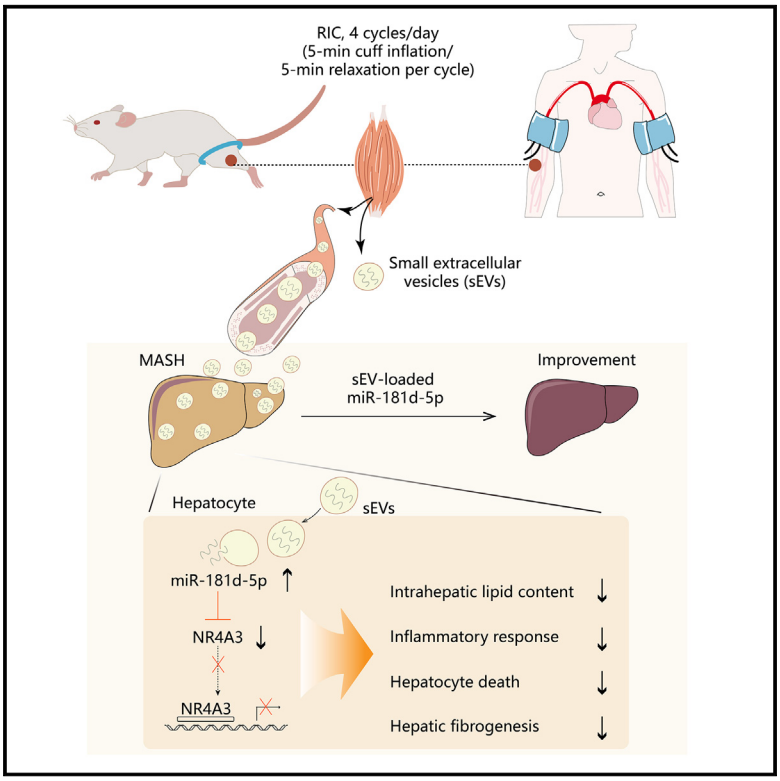

Highlights

- Chronic RIC treatment significantly alleviates MASH
- Muscle-derived sEVs mediate the benefits of RIC by transporting miR-181d-5p
- Hepatic miR-181d-5p overexpression mirrors the anti-MASH effects of RIC
- EVs from RIC-treated humans recapitulate the benefits of RIC in mice

Authors

Yichao Zhao, Ling Gao, Jianqing Chen, ..., Kun Qian, Alex F. Chen, Jun Pu

Correspondence

pujun310@hotmail.com

In brief

Remote limb ischemic conditioning (RIC) alleviates steatohepatitis. Zhao et al. report that RIC treatment alleviates metabolic dysfunction-associated steatohepatitis (MASH). Muscle-to-liver transfer of small extracellular vesicles (sEVs) mediated the anti-MASH effect of chronic RIC treatment. EV-loaded miR-181d-5p improved MASH phenotypes by suppressing its target nuclear receptor 4A3.

Zhao et al., 2025, Cell Metabolism *37*, 886–902
April 1, 2025
https://doi.org/10.1016/j.cmet.2025.02.009

CellPress

CellPress

Cell Metabolism

Article

Remote limb ischemic conditioning alleviates steatohepatitis via extracellular vesicle-mediated muscle-liver crosstalk

Yichao Zhao,[1,8] Ling Gao,[2,8] Jianqing Chen,[3,8] Jingze Wei,[3,8] Guanqiao Lin,[1] Kewei Hu,[3] Wubin Zhao,[1] Weijun Wei,[4] Wei Huang,[5] Lingchen Gao,[1] Ancai Yuan,[1] Kun Qian,[1,6] Alex F. Chen,[7] and Jun Pu[1,3,9,*]

[1]Division of Cardiology, State Key Laboratory of Systems Medicine for Cancer, Renji Hospital, School of Medicine, Shanghai Jiao Tong University, Shanghai, China

[2]Obstetrics and Gynecology Hospital, Institute of Reproduction and Development, Fudan University, Shanghai, China

[3]Graduate School of Bengbu Medical College, Bengbu, Anhui, China

[4]Department of Nuclear Medicine, Institute of Clinical Nuclear Medicine, Renji Hospital, School of Medicine, Shanghai Jiao Tong University, Shanghai, China

[5]Department of Radiation Oncology, Renji Hospital, School of Medicine, Shanghai Jiao Tong University, Shanghai, China

[6]School of Biomedical Engineering, Institute of Medical Robotics and Institute of Translational Medicine, Shanghai Jiao Tong University, Shanghai, China

[7]Institute for Developmental and Regenerative Cardiovascular Medicine, Xinhua Hospital, Shanghai Jiao Tong University School of Medicine, Shanghai, China

[8]These authors contributed equally

[9]Lead contact

*Correspondence: pujun310@hotmail.com

https://doi.org/10.1016/j.cmet.2025.02.009

SUMMARY

Metabolic dysfunction-associated steatohepatitis (MASH) is an advanced form of liver disease with adverse outcomes. Manipulating interorgan communication is considered a promising strategy for managing metabolic disease, including steatohepatitis. Here, we report that remote limb ischemic conditioning (RIC), a clinically validated therapy for distant organ protection by transient muscle ischemia, significantly alleviated steatohepatitis in different mouse models. The beneficial effect of limb ischemic conditioning was mediated by muscle-to-liver transfer of small extracellular vesicles (sEVs) and their cargo microRNAs, leading to elevation of miR-181d-5p in the liver. Hepatic miR-181d-5p overexpression faithfully mirrored the molecular and histological benefits of limb ischemic conditioning by suppressing nuclear receptor 4A3 (NR4A3). Furthermore, circulating EVs from human volunteers undergoing limb ischemic conditioning improved steatohepatitis and transcriptomic perturbations in primary human hepatocytes and animal models. Our data underscore the translational potential of limb ischemic conditioning for steatohepatitis management and extend our understanding of muscle-liver crosstalk.

INTRODUCTION

Metabolic dysfunction-associated fatty liver disease (MAFLD) is affecting approximately one-third of adults.[1] MAFLD consists of a spectrum of disease states ranging from simple steatosis to metabolic dysfunction-associated steatohepatitis (MASH). MASH is an aggressive form of MAFLD, characterized by the presence of inflammatory infiltration, hepatocyte injury, and varying degrees of fibrosis.[2] MASH significantly heightens the risks of end-stage liver disease and is anticipated to become the primary cause of liver transplantation in the forthcoming decade.[3] In addition, individuals with MASH face elevated risks of cardiovascular disease, the leading cause of death in this patient population.[4] Despite these clinical burdens and the prevalence of MASH, this condition remains an unmet clinical need.

Beyond the intrinsic hepatic mechanisms, the substantial roles of organ communication in the pathogenesis of MASH are well-established.[5] Leveraging interorgan communication (e.g., gut-liver, muscle-liver, adipose tissue-liver, etc.) is considered a promising strategy for MASH treatment.[6] In particular, the benefits of manipulating muscle-liver interaction are most well reflected by the anti-steatosis effects of physical exercise.[7] Despite its health benefits,[8] participation in exercise is disappointingly low in the general population and patients,[9] due to constraints including time and facilities.[10] Interestingly, remote limb ischemic conditioning (RIC), a clinically validated therapy for remote organ protection by noninvasive muscle treatment, has demonstrated many health benefits akin to exercise, such as improved sport performance and post-stroke rehabilitation.[11,12] RIC treatment is easy and safe, involving brief,

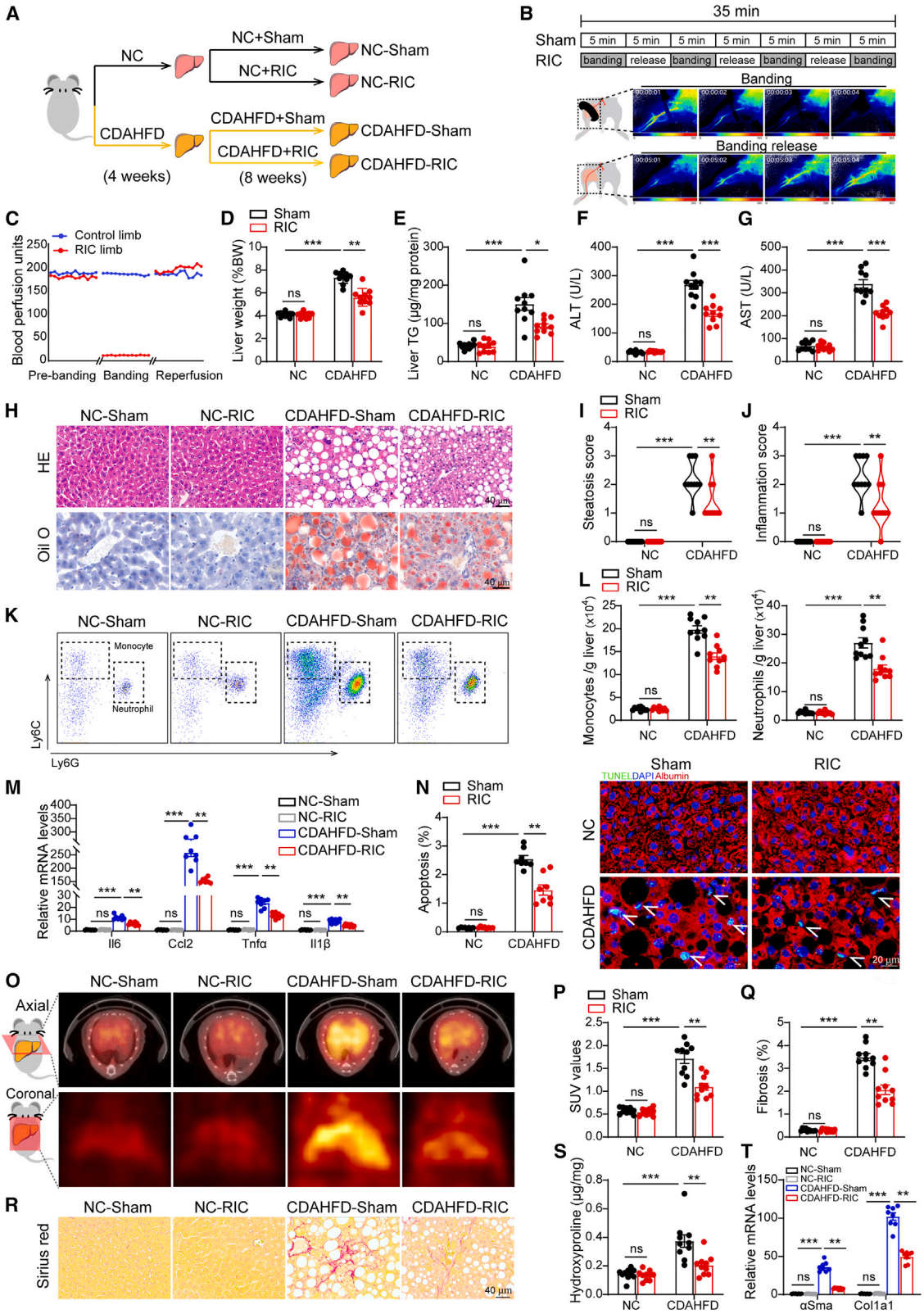

Figure 1. Chronic RIC treatment ameliorates liver steatosis, inflammation, and fibrosis in a MASH model induced by a CDAHFD

(A) Schematic illustration showing the study protocol.

(B) The RIC protocol and dynamic laser Doppler perfusion images of hindlimb ischemia and reperfusion during an RIC treatment.

(legend continued on next page)

reversible episodes of limb ischemia using blood pressure cuffs in humans.[13] RIC is widely applied for protection against ischemic injuries in distant organs.[13] Interestingly, mechanistic explorations in both clinical and animal studies revealed metabolic benefits of RIC treatment in ischemic heart and brain tissues.[14] In a cohort of 173 patients undergoing coronary artery grafting, RIC treatment significantly improved mitochondrial metabolism in heart tissues.[14] These findings strongly support the hypothesis that chronic RIC treatment may confer beneficial effects in the management of metabolic diseases. However, the effects of RIC treatment in metabolic disorders remain unexplored, including MASH and others.

In this study, we investigated the effects of RIC treatment in MASH models and explored its potential translational significance through the inclusion of human volunteers. Chronic RIC treatment effectively attenuated hepatic steatosis, inflammation, and fibrogenesis in both choline-deficient, L-amino acid-defined, high-fat diet (CDAHFD) and high-fat and high-cholesterol (HFHC) diet-induced MASH models in mice. Mechanistically, RIC treatment increased miR-181d-5p levels in the liver via transfer of muscle-derived small extracellular vesicles (sEVs). Hepatic miR-181d-5p overexpression mimicked the protective effects of RIC treatment by suppressing the transcription factor nuclear receptor 4A3 (NR4A3). Moreover, circulating sEVs obtained from human volunteers undergoing RIC treatment ameliorated MASH phenotypes in mouse models and primary human hepatocytes. Collectively, our study suggests that RIC treatment holds translatable therapeutic potential in the management of MASH.

RESULTS

Chronic RIC treatment ameliorates MASH phenotypes in mouse models

We initially investigated the effects of RIC treatment in a MASH model induced by a CDAHFD feeding. Mice were first subjected to a CDAHFD for 4 weeks (when MASH phenotypes appear),[15] followed by RIC treatment (4 cycles of 5-min limb ischemia/5-min reperfusion daily) for an additional 8 weeks (Figure 1A). Successful induction of RIC treatment was confirmed via laser Doppler perfusion imaging (Figures 1B and 1C). Compared with sham treatment, RIC treatment significantly reduced liver weight (Figure 1D) and intrahepatic lipid accumulation (Figure 1E). Hepatic function also showed improvement with RIC treatment, indicated by reduced plasma alanine aminotransferase (ALT) and aspartate aminotransferase (AST) levels when compared to those of the sham group (Figures 1F and 1G). Consistent with biochemical results, histological results suggested reduced hepatic steatosis scores by RIC treatment (Figures 1H and 1I). Additionally, RIC treatment decreased hepatic inflammation scores, myeloid cell infiltration, and inflammatory cytokine expression (Figures 1J–1M), accompanied by reduced hepatocellular death (Figure 1N). Furthermore, we designed a positron emission tomography (PET) imaging tracer of fibroblast activation protein inhibitor (FAPI),[16] which allows *in vivo* visualization of hepatic fibrosis.[17] PET imaging results showed a significant reduction in hepatic FAPI signals in models treated with RIC (Figures 1O and 1P), indicating attenuated hepatic fibrosis. This was consistent with decreased Sirius red positive areas, hydroxyproline content, and transcription levels of fibrotic genes (Figures 1Q–1T). These protective effects of RIC were not associated with changes in food intake or physical activities (Figure S1). Considering the sex differences in MASH development,[18] we further evaluated the effects of RIC treatment on MASH phenotypes in female mice. Similar to findings in male mice, RIC treatment significantly attenuated CDAHFD-induced MASH progression in female mice (Figure S2).

We then conducted RNA sequencing (RNA-seq) analysis on liver tissues to explore the molecular impact of RIC treatment in MASH. Principal-component analysis (PCA) demonstrated clear separation between RIC-treated and sham-treated MASH groups, while normal chow (NC) groups clustered together (Figure 2A). Consistent with PCA results, RIC treatment induced significant changes in global gene expression in MASH (Figures 2B and 2C). Enrichment analysis of differentially expressed genes (DEGs) indicated that upregulated genes by RIC treatment were primarily involved in lipid metabolism, while downregulated genes were enriched in inflammatory response, fibrotic signaling, and apoptosis pathways (Figures 2D and 2E). In addition to DEG enrichment results, gene set enrichment analysis (GSEA) using the entire transcriptomic dataset confirmed the upregulation of lipid catabolism (e.g., fatty acid β-oxidation and perxisome) and the suppression of inflammation, fibrosis, and cell injury (e.g., tumor necrosis factor alpha [TNF-α] signaling

(C) Representative dynamic blood flow measurements for a hindlimb during RIC treatment.
(D–G) Comparison of liver weight/body weight ratios, hepatic TG contents, and serum levels of ALT and AST among indicated groups (n = 10 mice per group).
(H) Representative H&E and oil red O staining images of liver sections in indicated groups. Scale bar represents 40 μm.
(I and J) Steatosis scores and inflammation scores based on histological staining in indicated groups (n = 10 mice per group).
(K) Images of flow cytometry results showing monocyte and neutrophil numbers in liver tissues in indicated groups.
(L) Quantitative analysis of monocyte and neutrophil numbers in liver tissues in indicated groups (n = 10 mice per group).
(M) Expression of inflammatory genes in liver tissues in indicated groups (n = 8 mice per group).
(N) TUNEL staining results and quantitative analysis of hepatocellular apoptosis in indicated groups (n = 8 mice per group). Scale bar represents 20 μm.
(O) Coronal and axial images of [^{68}Ga]Ga-DOTA-FAPI PET/CT scanning in indicated groups.
(P) Quantitative analysis of [^{68}Ga]Ga-DOTA-FAPI signals in livers in indicated groups (n = 10 mice per group).
(Q and R) Representative Sirius red staining images of liver sections and quantitative analysis of fibrotic areas in the liver in indicated groups (n = 10 mice per group). Scale bar represents 40 μm.
(S) The hydroxyproline content of the liver was determined in indicated groups (n = 10 mice per group).
(T) Expression of fibrotic markers in indicated groups (n = 8 mice per group). $^{*}p < 0.05$, $^{**}p < 0.01$, $^{***}p < 0.001$. Abbreviations: ALT, alanine aminotransferase; αSMA, alpha smooth muscle actin; AST, aspartate aminotransferase; BW, body weight; Ccl2, chemokine (C-C motif) ligand 2; CDAHFD, choline-deficient, L-amino acid-defined, high-fat diet; Col1a1, collagen type I alpha 1; FAPI, fibroblast activation protein inhibitor; Il-1β, interleukin-1 beta; Il-6, interleukin-6; MASH, metabolic dysfunction-associated steatohepatitis; NC, normal chow; PET/CT, positron emission tomography/computed tomography; RIC, remote limb ischemic conditioning; SUV, standardized uptake value; TG, triglyceride; Tnf-α, tumor necrosis factor alpha; TUNEL, terminal deoxynucleotidyl transferase dUTP nick-end labeling.

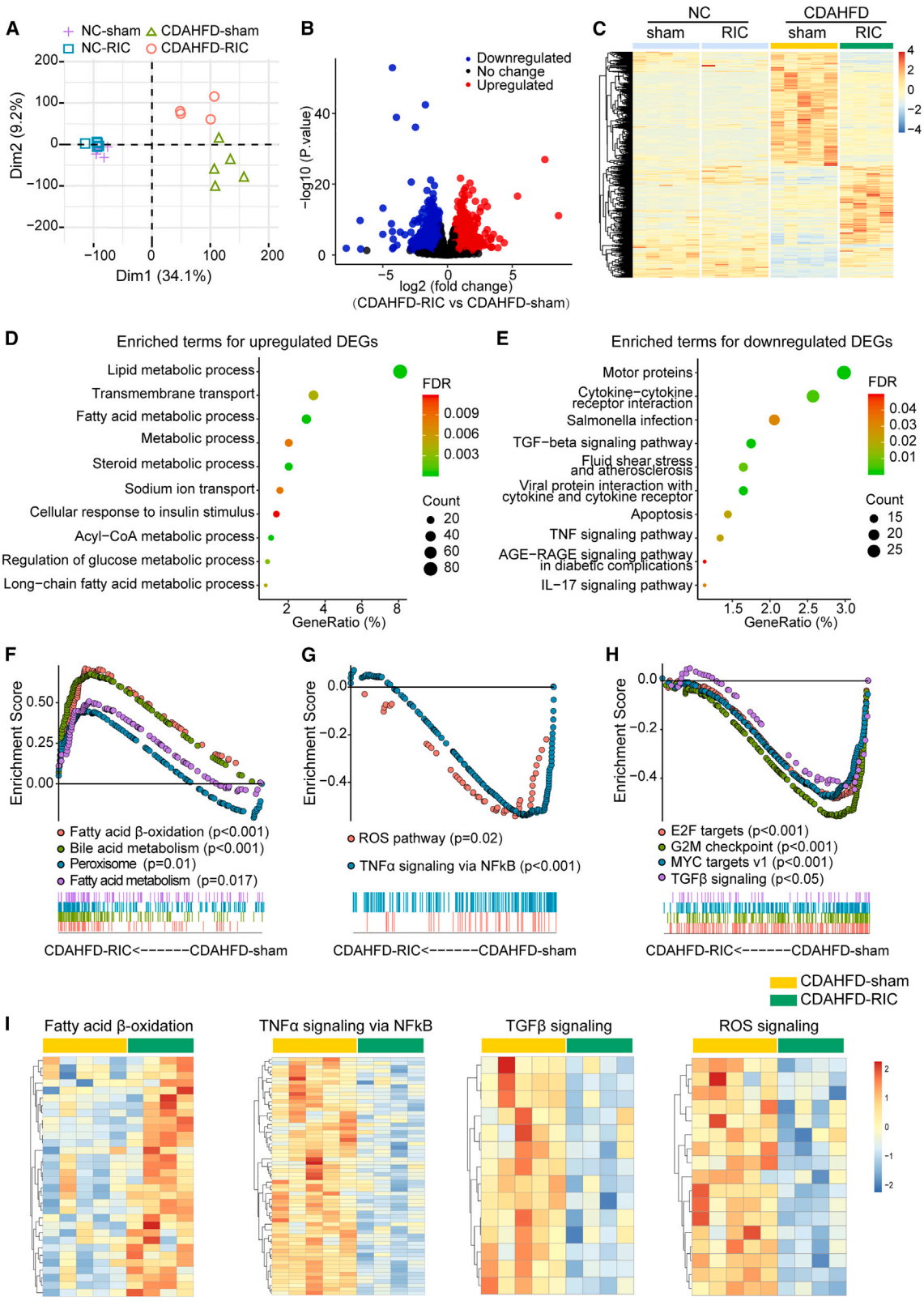

Figure 2. Chronic RIC treatment leads to transcriptomic reprogramming in the liver favoring MASH alleviation

(A) RNA sequencing (RNA-seq) was performed to compare gene expression in liver tissues. PCA suggested clear separation between RIC-treated and sham-treated MASH models (n = 4–5 mice per group; samples failing to pass quality control were excluded).

(legend continued on next page)

via nuclear factor κB [NF-κB], transforming growth factor β [TGF-β] signaling, and reactive oxidative stress) in RIC-treated MASH group (Figures 2F–2I). These results from unbiased global transcriptomic analysis corroborated the anti-MASH effects of RIC treatment.

To further confirm the protective effects of RIC treatment in MASH, we established an additional MASH model induced by an HFHC diet. RIC treatment commenced 10 weeks after initiating HFHC feeding (a time point commonly used to initiate testing therapies)[19] and continued for 8 weeks (Figure S3A). Different from the dominant macrovesicular steatosis induced by CDAHFD feeding (large lipid vacuoles pushing the nucleus to the cell periphery), HFHC models presented a mix of macrovesicular and microvesicular steatosis (multiple lipid vacuoles surrounding a central nucleus) (Figure S3F). Despite the difference, RIC treatment significantly reduced liver weight, triglyceride (TG) accumulation in the liver, and serum levels of ALT and AST (Figures S3B–S3E). Additionally, histological and molecular analysis results confirmed significant improvements in hepatic steatosis, inflammatory response, and fibrosis (Figures S3F–S3N), concomitant with reduced hepatocyte death (Figure S3O).

Chronic RIC treatment alleviates MASH phenotypes via circulating mediators

To test whether chronic RIC treatment protects against MASH via circulating factors, we established parabiosis models (two combined mice with shared circulation). After 4 weeks of CDAHFD feeding, all the left parabionts within the parabiosis models underwent either RIC or sham treatment for an additional 8 weeks, while all the right parabionts were sampled for phenotypic assessment (Figure 3A). Before the commencement of RIC treatment, shared circulation in the parabiosis models was confirmed by observing the transferred Evans blue dye between the paired mice (Figure 3B). Compared with sham treatment, RIC treatment to one parabiont resulted in improved MASH phenotypes in its paired partner, notably reducing liver steatosis, fibrosis, and inflammation (Figures 3C–3K). Meanwhile, flow cytometry confirmed a significant decrease in inflammatory monocyte and neutrophil infiltration in the liver by RIC treatment (Figures 3L and 3M), as well as reduced hepatocyte apoptosis (Figure 3N). The changes in inflammatory cell infiltration might stem from altered supply of immune cells in the circulation or changed chemoattraction.[20] Flow cytometry analysis revealed comparable numbers of circulating neutrophils and monocytes between the two groups (Figures S4A–S4D). Meanwhile, neutrophil and monocyte numbers in hematopoietic organs, including the spleen and bone marrow, were similar between the two groups (Figures S4E–S4H). These findings suggest minimal changes in circulating myeloid cell supply due to RIC treatment in MASH. By contrast, we observed that expression levels of chemokines and adhesion molecules were significantly reduced in the fatty livers by RIC treatment (Figure S4I), suggesting suppressed chemoattraction. Together, these results indicate that the protective effect of RIC treatment is conveyed through circulation, independent of circulating immune cell supply.

sEVs secreted from RIC-treated hindlimb muscles alleviate MASH phenotypes

To identify the circulating factors responsible for the benefits of RIC treatment in MASH, we first validated the protective effects of plasma from RIC-treated mice (RIC-conditioned plasma) in steatotic primary mouse hepatocytes induced by palmitic acid (PA) (Figure S5A). Compared with plasma from control mice, RIC-conditioned plasma dose-dependently reduced lactate dehydrogenase (LDH) release in PA-treated primary mouse hepatocytes (Figure S5B), indicating attenuated cell injury. Consistently, RIC-conditioned plasma reduced PA-induced hepatocyte apoptosis and preserved mitochondrial membrane potential in comparison to control mouse plasma (Figures S5C–S5E). Additionally, RIC-conditioned plasma improved lipid metabolism (Figures S5F–S5H) and reduced inflammatory cytokine expression levels (Figure S5I). sEVs play a crucial role as messengers in interorgan communication.[21] We then separated sEVs and EV-free fractions from plasma and tested their individual effects in mouse hepatocytes. sEVs were isolated by the ultracentrifugation approach and characterized using nanoparticle tracking analysis (NTA) and transmission electron microscopy (TEM) (Figure S6A). RIC treatment slightly increased concentrations of plasma sEVs (Figure S6B). Western blot (WB) analysis revealed the presence of EV markers (TSG101, CD63, and CD9) and the absence of negative markers of EVs (calnexin and GM130) in sEVs (Figure S6C). RIC-conditioned sEVs but not EV-free plasma reduced LDH release in PA-treated primary mouse hepatocytes, compared with control treatment (Figures S6D and S6E). Moreover, RIC-conditioned sEVs but not EV-free plasma inhibited cellular apoptosis, lipid accumulation, and inflammatory cytokine production in PA-treated hepatocytes (Figures S6F–S6R). These results suggest that circulating sEVs from RIC-treated mice protected against lipotoxic injury in hepatocytes.

Muscle-derived sEVs (mEVs) can disseminate through circulation and enter remote organs with a high enrichment in the liver.[22,23] We hypothesized that the therapeutic sEVs were originating from RIC-treated hindlimb muscles. We then isolated mEVs through size exclusion chromatography and characterized mEVs via NTA, TEM, and WB analysis (Figures 4A–4C). Incubation with green lipophilic fluorescent dye (PKH67)-labeled mEVs indicated the uptake of mEVs by primary hepatocytes (Figure 4D). After injection of 1,1′-dioctadecyl-3,3,3′,3′-tetramethylindotricarbocyanine iodide (DIR)-labeled mEVs in mice, *in vivo* bioluminescence imaging indicated enrichment of mEVs in the liver

(B) Volcano plot of the RNA-seq results showing differentially expressed genes (DEGs) (n = 4–5 mice per group). The red dots represent significantly upregulated genes, and the blue dots represent significantly downregulated genes.
(C) Heatmap plot showing the relative expression of DEGs across the four indicated groups.
(D and E) Enrichment analysis results using the upregulated DEGs (D) or the downregulated DEGs (E).
(F–H) GSEA results using the entire RNA-seq dataset.
(I) Heatmap plots showing the relative gene expression enriched in indicated pathways. Abbreviations: CDAHFD, choline-deficient, L-amino acid-defined, high-fat diet; DEGs, differentially expressed genes; MASH, metabolic dysfunction-associated steatohepatitis; NC, normal chow; RIC, remote limb ischemic conditioning.

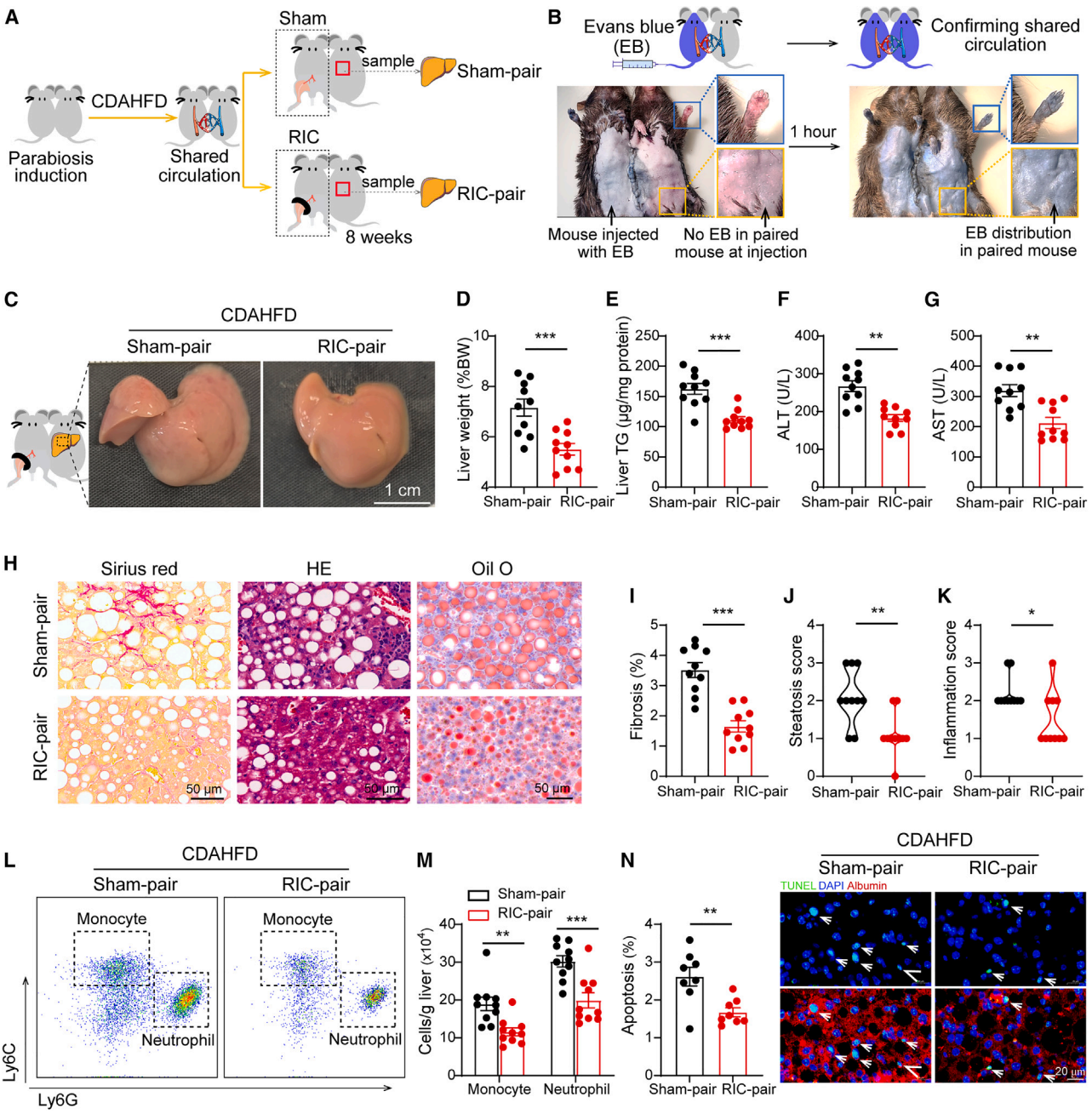

Figure 3. Circulating factors contribute to the anti-MASH effects of chronic RIC treatment

(A) Schematic illustration showing the study protocol.

(B) Shared circulation in the parabiosis models was confirmed by observing the transferred Evans blue dye between the paired mice.

(C) Gross morphology of livers in the indicated groups.

(D–G) Comparison of liver weight/body weight ratios, hepatic triglyceride contents, and serum levels of ALT and AST among indicated groups (n = 10 mice per group).

(H) Representative H&E, Sirius red, and oil red O staining images from indicated groups. Scale bar represents 50 μm.

(I–K) Quantitative analysis of fibrotic areas in the liver, steatosis scores, and inflammation scores based on histological staining results in indicated groups (n = 10 mice per group).

(L) Images of flow cytometry results showing monocytes and neutrophils in liver tissues in indicated groups.

(M) Quantitative analysis of monocyte and neutrophil numbers in liver tissues in indicated groups (n = 10 mice per group).

(N) TUNEL staining results and quantitative analysis of hepatocellular apoptosis in indicated groups (n = 8 mice per group). Scale bar represents 20 μm. Statistical analysis was performed by Student's t test or Mann-Whitney U test. *p < 0.05, **p < 0.01, ***p < 0.001. Abbreviations: ALT, alanine aminotransferase; AST, aspartate aminotransferase; BW, body weight; CDAHFD, choline-deficient, L-amino acid-defined, high-fat diet; MASH, metabolic dysfunction-associated steatohepatitis; RIC, remote limb ischemic conditioning; TG, triglyceride; TUNEL, terminal deoxynucleotidyl transferase dUTP nick-end labeling.

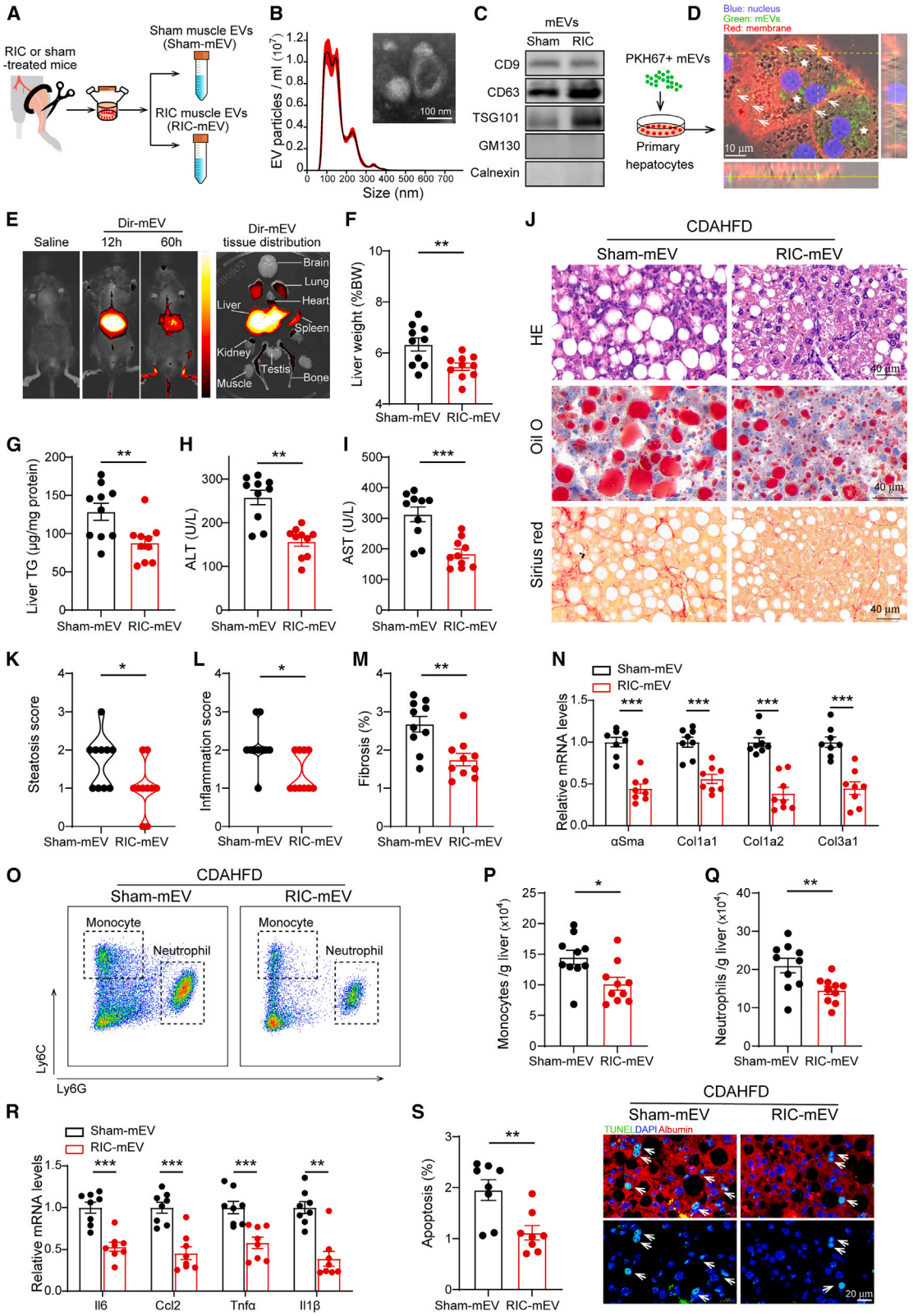

Figure 4. Administration of mEVs from RIC-treated mice improves MASH phenotypes

(A) Illustration showing sEVs collection from hindlimb muscles.

(B) Size distribution of muscle-derived EVs (mEVs) determined by NTA, and their morphology characterized by TEM.

(legend continued on next page)

(Figure 4E). RIC-conditioned mEVs dose-dependently reduced LDH release in PA-treated primary mouse hepatocytes (Figure S7A) and significantly mitigated PA-induced cellular apoptosis, inflammatory cytokine production, and promoted fatty acid oxidation in primary hepatocytes, in comparison to control mEV treatment (Figures S7B–S7H). Based on these *in vitro* results, we evaluated the effects of RIC-conditioned mEVs in diet-induced MASH models. We observed that RIC-conditioned mEV administration (1×10^{10} particles/once weekly) significantly improved MASH phenotypes compared with control mEV treatment in both CDAHFD and HFHC models (Figures 4F–4S and S8). To explore whether mEV secretion from muscles contributes to the beneficial effects of RIC treatment *in vivo*, a muscle-specific Rab27a knockout (KO) mouse strain was used (Figures S9A and S9B), as Rab27a deficiency impedes EV secretion[24] (Figure S9C). Blockade of muscle EV secretion by Rab27a deletion compromised the protective effects of RIC treatment on MASH (Figures S9D–S9Q). Together, these results suggest that mEVs contribute to the anti-MASH effects of chronic RIC treatment.

sEV-loaded miR-181d-5p contributes to the protective effects of RIC treatment in MASH

The microRNAs (miRNAs) carried by sEVs play crucial roles in influencing recipient organs.[21,25] To investigate the potential contribution of encapsulated miRNAs to the protective effects of mEVs derived from RIC-treated muscle, we disrupted miRNA expression in the hindlimb by injecting adeno-associated viruses (AAVs) expressing small interfering RNA (siRNA) targeting Dicer (AAV-shDicer), an enzyme crucial for miRNA processing[26] (Figure S10A). At 2 weeks after injection, AAV-siDicer effectively suppressed Dicer expression in muscle tissues (Figures S10B–S10D). Disruption of miRNAs by AAV-shDicer injection in hindlimb diminished the protective effects of RIC-conditioned mEVs in steatotic primary mouse hepatocytes (Figures S10E–S10L). Furthermore, disruption of sEV-loaded miRNAs notably diminished the favorable effects of RIC-conditioned mEVs on MASH phenotypes *in vivo* (Figure S11). These results indicate that sEV-loaded miRNAs contributed to the benefits of RIC-conditioned sEV treatment in MASH.

To uncover the specific sEV-loaded miRNAs contributing to the benefits of RIC against MASH, we conducted miRNA sequencing on circulating sEVs. We identified ten significantly upregulated miRNAs (fold change > 1.5, $p < 0.05$) in circulating sEVs from RIC-treated mice compared with sham-treated mice (Figures 5A and 5B). Subsequently, we assessed the expression of these ten miRNAs in both muscle and liver tissues in CDAHFD models. Among them, miR-181d-5p, miR-466a-3p, and miR-669a-3p were concurrently upregulated in both muscle and liver tissues by RIC treatment (Figures 5C and 5D). Consistently, PCR analysis confirmed that these three miRNAs were elevated in RIC-conditioned mEVs compared with control mEVs (Figure 5E). However, in the liver of muscle-specific Rab27a KO mice, these three miRNAs were not increased by RIC treatment, though these miRNAs were elevated by RIC in muscle tissues (Figure 5F), indicating the crucial role of mEVs in elevating these miRNAs in the liver. We then investigated the functions of these candidate miRNAs using miRNA mimics. miRNA-181d-5p mimics (10 nM) significantly reduced cellular death and inflammatory response and increased fatty acid oxidation in PA-treated primary mouse hepatocytes compared with control mimics (Figure S12). However, miR-466a-3p and miR-669a-3p mimics exhibited limited effects on lipotoxic injury in primary mouse hepatocytes (Figure S12). The anti-steatotic effects of miRNA-181d-5p were further confirmed in primary human hepatocytes (Figure S13).

We further explored the therapeutic potential of miRNA-181d-5p overexpression on MASH phenotypes *in vivo* (Figure 5G). Hepatocyte-specific miRNA-181d-5p overexpression was induced by intravenous injection of AAV serotype 8 (AAV8) driven by a liver-specific thyroxine-binding globulin promoter. The specificity of this gene expression approach to the liver and hepatocytes was validated (Figures S14A–S14C). Compared with control AAV injection, AAVs encoding miRNA-181d-5p (AAV-181d) increased hepatic miRNA-181d-5p expression (Figures 5H and S14D) and significantly alleviated liver steatosis, immune infiltration, and hepatic fibrosis in both CDAHFD (Figures 5I–5S) and HFHC models (Figures S14E–S14P). Overexpression of miRNA-181d-5p significantly changed transcriptomic patterns in MASH (Figure 5T). Intriguingly, GSEA results indicated that miRNA-181d-5p overexpression mirrored the effects of RIC treatment on hepatic

(C) The characterization of sEV positive and negative markers, including CD63, TSG101, CD9, GM130, and calnexin.
(D) Incubation with PKH67-labeled mEVs indicated the uptake of mEVs by primary hepatocytes. Arrows indicate sEVs fused with the plasma membrane, and asterisks indicate internalized sEVs. Scale bar represents 10 μm.
(E) Mice were intravenously injected with saline or DIR-labeled mEVs. Bioluminescence imaging results showing tissue distribution at 12 and 60 h after mEV injection.
(F–I) Comparison of liver weight/body weight ratios, hepatic triglyceride contents, and serum levels of ALT and AST between indicated groups (n = 10 mice per group).
(J) Representative H&E, Sirius red, and oil red O staining images of liver sections in indicated groups. Scale bar represents 40 μm.
(K and L) Steatosis scores and inflammation scores based on histological staining results in indicated groups (n = 10 mice per group).
(M) Quantitative analysis of fibrotic areas in the liver in indicated groups (n = 10 mice per group).
(N) Expression of fibrotic markers in indicated groups (n = 8 mice per group).
(O) Images of flow cytometry results showing monocyte and neutrophil numbers in liver tissues in indicated groups.
(P and Q) Quantitative analysis of monocyte and neutrophil numbers in liver tissues in indicated groups (n = 10 mice per group).
(R) Expression of inflammatory genes in liver tissues in indicated groups (n = 8 mice per group).
(S) TUNEL staining results and quantitative analysis of hepatocellular apoptosis in indicated groups (n = 8 mice per group). Scale bar represents 20 μm. Statistical analysis was performed by Student's t test or Mann-Whitney U test. *$p < 0.05$, **$p < 0.01$, ***$p < 0.001$. Abbreviations: ALT, alanine aminotransferase; αSMA, alpha smooth muscle actin; AST, aspartate aminotransferase; BW, body weight; Ccl2, chemokine (C-C motif) ligand 2; CDAHFD, choline-deficient, L-amino acid-defined, high-fat diet; Col1a1, collagen type I alpha 1; Col1a2, collagen type I alpha 2; Col3a1, collagen type III alpha 1; Il-1β, interleukin-1 beta; Il-6, interleukin-6; mEVs, muscle-derived extracellular vesicles; MASH, metabolic dysfunction-associated steatohepatitis; RIC, remote limb ischemic conditioning; TG, triglyceride; Tnf-α, tumor necrosis factor alpha; TUNEL, terminal deoxynucleotidyl transferase dUTP nick-end labeling.

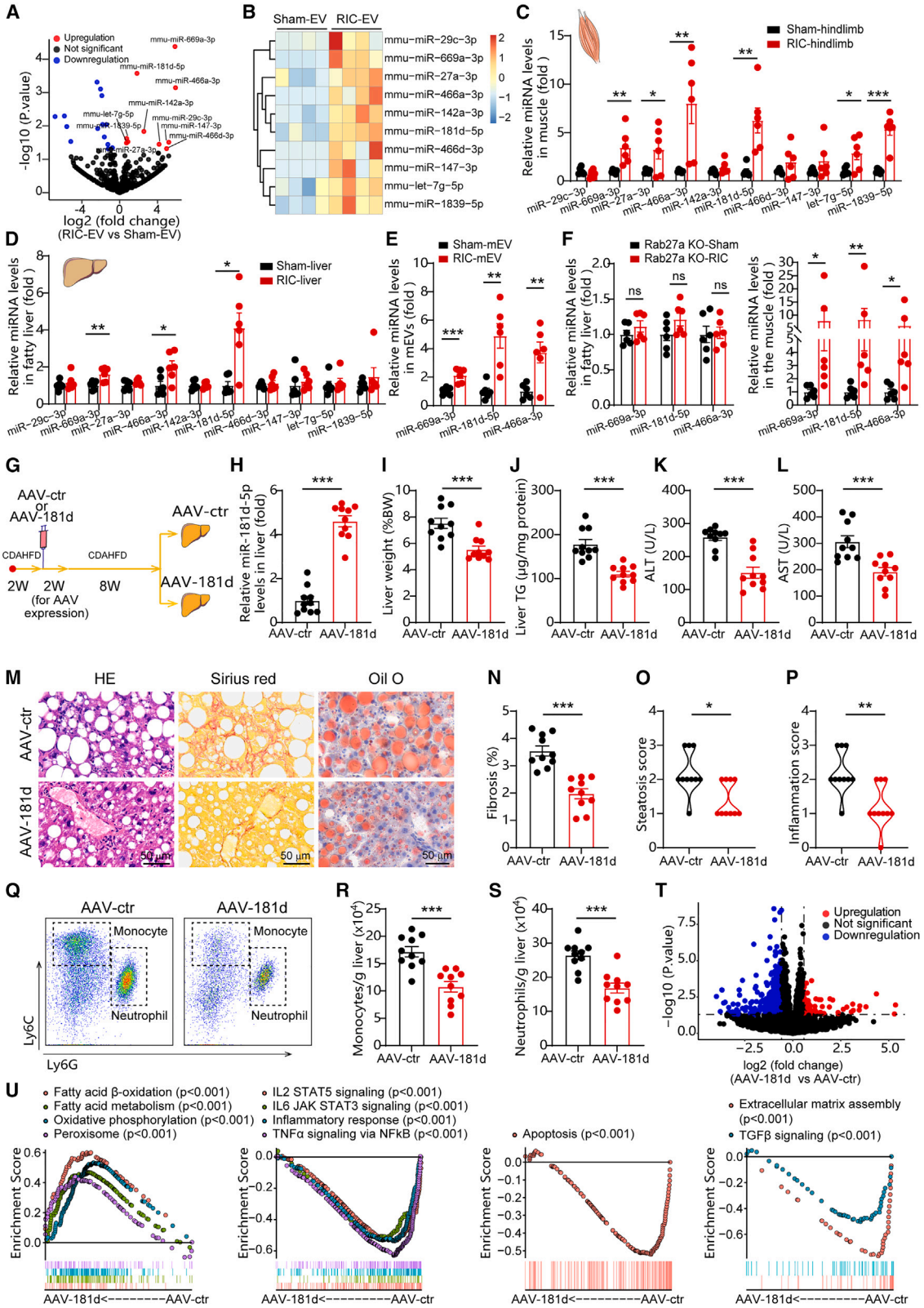

Figure 5. sEV-loaded miR-181d-5p contributes to the protective effects of RIC treatment in MASH

(A) Volcano plot of the miRNA-seq results showing differentially expressed miRNAs in circulating sEVs from RIC-treated and sham-treated mice (n = 4 samples per group).

(legend continued on next page)

transcriptomic changes. Consistent with the observations in RIC-treated mice (Figure 2), miRNA-181d-5p overexpression in liver led to upregulated gene sets associated with fatty acid catabolism (i.e., fatty acid β-oxidation, oxidative phosphorylation, and peroxisome) and suppressed gene sets related to inflammation, apoptosis, and fibrosis (i.e., inflammatory response, TNF-α signaling via NF-κB, TGF-β signaling, extracellular matrix assembly, and apoptosis) (Figure 5U).

To ascertain the contribution of miRNA-181d-5p to the protective effects of RIC treatment in MASH, we antagonized miRNA-181d-5p functions in the liver by inducing miRNA-181d-5p sponge overexpression through AAV injection (Figure S15A). In mice injected with control AAVs, chronic RIC treatment significantly ameliorated MASH phenotypes compared with sham treatment (Figures S15B–S15L). However, hepatic expression of miRNA-181d-5p sponge reversed the protective effects of RIC treatment in MASH (Figures S15B–S15L). Together, these data indicate that the anti-MASH effects of RIC treatment are attributable to the transfer of sEV-loaded miR-181d-5p to the liver.

MiR-181d-5p suppressed MASH by targeting the transcription factor NR4A3

MiRNAs function by negatively modulating target gene expression.[21] Through the integration of downregulated genes by miR-181d-5p with common target genes predicted from TargetScan and MicroRNA Target Prediction Database (miRDB),[27,28] we identified eleven candidate target genes of miR-181d-5p. In the current model, we assumed that key target genes of miR-181d-5p would also exhibit decreased expression in RIC-treated mice since RIC treatment increased miR-181d-5p levels in the liver (Figure 5D). Upon further intersection with downregulated genes by RIC treatment, Nr4a3 emerged as the only potential direct target of miR-181d-5p (Figure 6A). PCR and WB analysis confirmed the suppression of hepatic NR4A3 by either miR-181d-5p overexpression or RIC-conditioned mEV injection in mice (Figures 6B–6E). Luciferase reporter assays confirmed direct targeting and suppression of Nr4a3 by miR-181d-5p mimics (Figure 6F). Conversely, Nr4a3 expression was significantly elevated in MASH liver samples compared with normal liver tissues (Figure 6G). Similarly, increased NR4A3 levels in human fatty liver samples were revealed by analysis of published datasets.[29] Moreover, cardiovascular studies reported pivotal roles of NR4A3 in promoting inflammatory response, oxidative stress, and cellular death,[30–32] underscoring the potential involvement of NR4A3 in MASH pathogenesis.

To investigate the role of NR4A3 in MASH, we generated a hepatocyte-specific Nr4a3 KO mouse strain (Figures S16A–S16C). At baseline, Nr4a3 KO mice exhibited similar body weight, glucose tolerance, insulin sensitivity, and serum lipid levels to wild-type littermates (Figures S16D–S16J). Additionally, liver histological analysis showed no overt hepatic phenotypes in hepatocyte-specific Nr4a3 KO mice at baseline (Figure S16K). We then tested the effects of Nr4a3 deficiency in a CDAHFD-induced MASH model (Figure 6H). Hepatocyte-specific Nr4a3 deletion significantly alleviated liver steatosis, collagen accumulation, and inflammation infiltration (Figures 6I–6Q). Meanwhile, Nr4a3 KO mice exhibited suppressed levels of inflammatory cytokines and fibrotic genes (Figures 6R and 6S). Moreover, Nr4a3 deletion significantly upregulated genes related to lipid catabolism (Figure 6T), including Sestrin2, a key factor known to alleviate lipotoxic liver injury by restraining mechanistic target of rapamycin complex 1 (mTOR1) and c-Jun N-terminal kinase (JNK) signalings.[33] Correspondingly, Nr4a3 deletion suppressed mTOR1/JNK signaling in the context of MASH (Figure 6U). Based on these results, we further explored whether Nr4a3 mediated the effects of miR-181d-5p and RIC-stimulated sEVs. To this end, we obtained hepatocytes expressing an miR-181d-5p-non-targetable mutant of Nr4a3 (Figures S17A and S17B). By the introduction of the non-targetable Nr4a3, RIC-stimulated mEVs failed to significantly mitigate PA-induced LDH release, lipid accumulation, and inflammation in hepatocytes. Additionally, miR-181d-5p mimics showed minimal beneficial effects in these PA-treated hepatocytes compared with control mimics (Figures S17C–S17K). These results suggest that inhibition of NR4A3 contributes to the protective role of miR-181d-5p in MASH.

Circulating sEVs from human volunteers undergoing RIC treatment alleviate MASH phenotypes

To explore the translational relevance of the animal findings, human volunteers were recruited and subjected to either RIC (4

(B) Heatmap plot showing the normalized counts of upregulated miRNAs in circulating sEVs from RIC-treated mice.
(C) PCR results showing the expression levels of the indicated miRNAs in hindlimb muscle tissues (n = 6 mice per group).
(D) PCR results showing the expression levels of the indicated miRNAs in liver tissues (n = 6 mice per group).
(E) PCR results showing the expression levels of the indicated miRNAs in mEVs (n = 6).
(F) PCR results showing the expression levels of the indicated miRNAs in livers (left) and hindlimb muscle tissues (right), from RIC-treated and sham-treated muscle-specific Rab27a KO mice (n = 6 mice per group).
(G) Schematic illustration showing the study protocol.
(H) Levels of miR-181d-5p expression in the livers from indicated groups (n = 10 mice per group).
(I–L) Comparison of liver weight/body weight ratios, hepatic triglyceride contents, and serum levels of ALT and AST between indicated MASH groups (n = 10 mice per group).
(M) Representative H&E, Sirius red, and oil red O staining images of liver sections in indicated groups. Scale bar represents 50 μm.
(N–P) Quantitative analysis of fibrotic areas in the liver, steatosis scores, and inflammation scores in indicated groups (n = 10 mice per group).
(Q) Images of flow cytometry results showing monocytes and neutrophils in liver tissues in indicated groups.
(R and S) Quantitative analysis of monocyte and neutrophil numbers in liver tissues in indicated groups (n = 10 mice per group).
(T) Volcano plot of the RNA-seq analysis on fatty liver tissues showing DEGs induced by miR-181d-5p overexpression (n = 5 mice per group).
(U) GSEA results showing significantly changed gene sets induced by miR-181d-5p overexpression. Statistical analysis was performed by Student's t test or Mann-Whitney U test. *$p < 0.05$, **$p < 0.01$, ***$p < 0.001$. Abbreviations: AAV-ctr, intravenous injection of control AAVs; AAV-181d, intravenous injection of AAVs encoding miR-181d-5p; ALT, alanine aminotransferase; AST, aspartate aminotransferase; BW, body weight; CDAHFD, choline-deficient, L-amino acid-defined, high-fat diet; mEVs, muscle-derived extracellular vesicles; MASH, metabolic dysfunction-associated steatohepatitis; RIC, remote limb ischemic conditioning; TG, triglyceride.

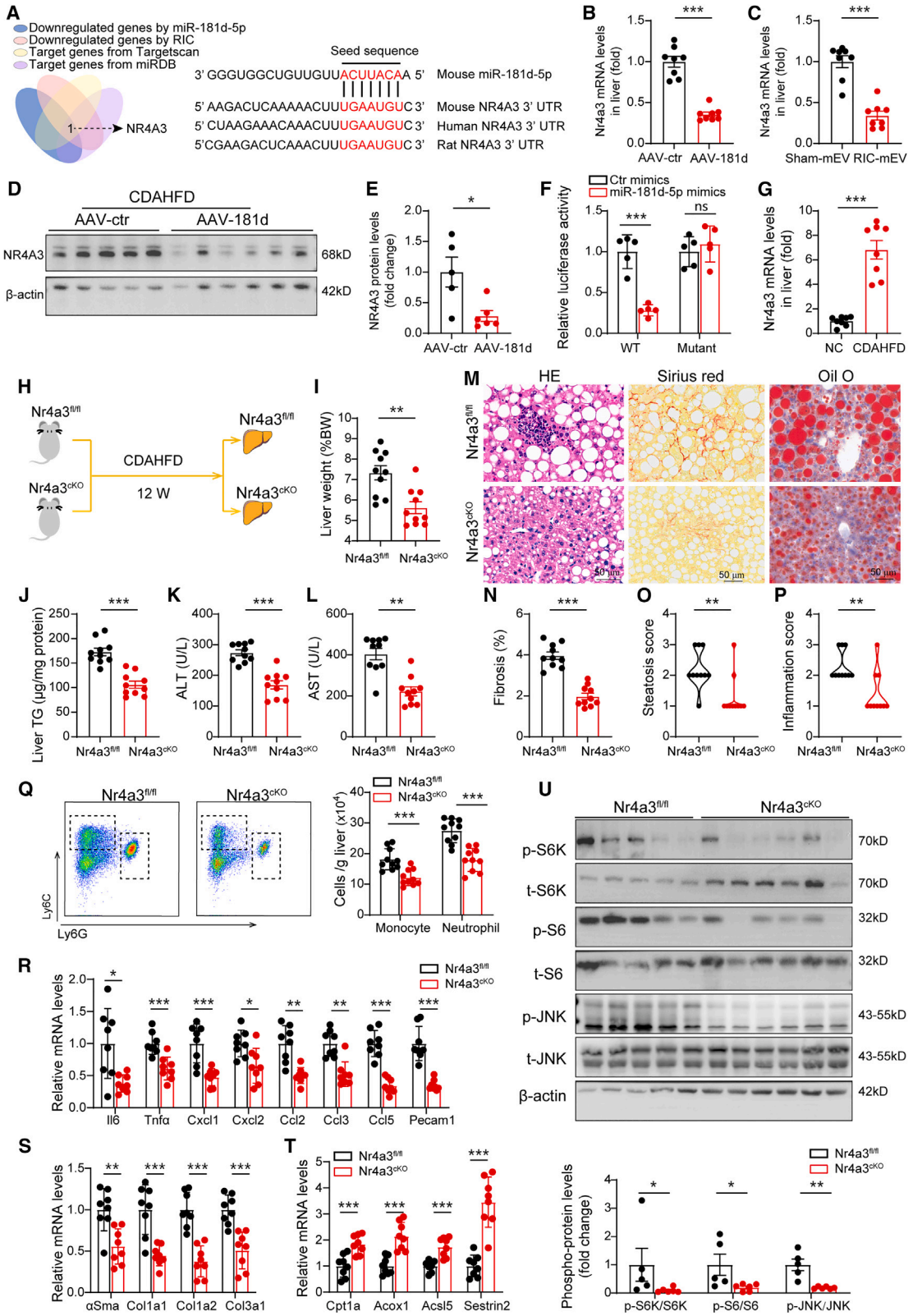

Figure 6. MiR-181d-5p suppressed MASH by targeting the transcription factor NR4A3

(A) A Venn diagram showing the screening of miR-181d-5p targets and sequence alignment between miR-181d-5p and the 3′ UTR of its target gene Nr4a3 in several species.

(legend continued on next page)

cycles of 5-min upper extremity ischemia/5-min reperfusion daily) or sham treatment with an automated RIC apparatus (Figures 7A and 7B; Table S1). Circulating sEVs were isolated from plasma (Figures S18A and S18B). Longitudinal analysis indicated that RIC but not sham treatment significantly increased miR-181d-5p content in human circulating sEVs compared with baseline (Figure S18C). Incubation with sEVs from volunteers undergoing RIC treatment (RIC-conditioned EVs) increased miR-181d-5p levels in primary human hepatocytes compared with control EV treatment (Figure S18D). Moreover, compared with control sEVs, RIC-conditioned human sEVs alleviated PA-induced cell death, steatosis, and inflammatory cytokine production in primary human hepatocytes (Figures S18E–S18L). Since injection of human plasma sEVs is well tolerated in animals, including mice, rats, and canis,[34,35] and the sEV-loaded human miR-181d-5p has the identical sequence with the mouse version, we further assessed the therapeutic potential of RIC-conditioned human EVs in MASH models (Figure 7C). Compared with control sEV treatment, RIC-conditioned human sEVs (3×10^{11} particles/day, once weekly) significantly improved MASH phenotypes in both CDAHFD (Figures 7D–7K) and HFHC diet-induced models (Figure S19). Notably, RIC-conditioned human sEVs induced transcriptomic changes in MASH (Figure 7L), which are akin to those by RIC treatment in fatty liver tissues: top upregulated gene sets were related to lipid catabolism, while downregulated gene sets were related to inflammation, fibrogenesis, and apoptosis (Figures 7M–7Q). These results indicate a potential anti-MASH effect of circulating sEVs from RIC-treated participants.

DISCUSSION

In this study, we documented previously unrecognized therapeutic effects of RIC treatment (a clinically validated therapy for ischemic injury in distant organs) on MASH phenotypes. Several novel contributions were made. First, through histological examination and unbiased RNA-seq analysis, we observed that chronic RIC treatment markedly mitigated hepatic steatosis, inflammation, and fibrosis in established MASH models induced by different dietary protocols. Second, mEVs played a crucial role in mediating the anti-MASH effects of RIC treatment by facilitating the transfer of sEV-loaded miR-181d-5p to the liver. Hepatic miR-181d-5p overexpression mirrored the transcriptomic changes and pathological improvements induced by RIC treatment in MASH. Third, the transcription factor NR4A3 is a target repressed by miR-181d-5p, and hepatocyte-specific NR4A3 deficiency significantly attenuated MASH progression. Finally, the administration of circulating sEVs from human volunteers subjected to RIC treatment improved MASH phenotypes and transcriptomic perturbations in animal models and primary human hepatocytes. These findings for the first time indicate the therapeutic potential of RIC treatment in a metabolic disorder and highlight the translational promise of RIC treatment in MASH management.

Organ crosstalk and intracellular communications are increasingly appreciated for their substantive roles in both disease progression and the maintenance of health.[5,6,20] Interconnected signaling pathways between the liver and diverse organs—muscle, adipose tissue, gut, and kidney—are pivotally involved in the pathogenesis of MAFLD.[5,6,36,37] Based on mechanistic understanding, promising therapeutic targets and strategies manipulating interorgan communication are emerging for MAFLD treatment, such as cholesterol metabolite supplementation that regulates gut-liver crosstalk.[6] Nevertheless, considerable groundwork is still required for many of these proposed therapies to progress into clinical trials. RIC is among a few organ crosstalk-manipulating therapies clinically validated for safety in patients and healthy volunteers.[13] RIC treatment is widely applied to protect remote infarcted organs (e.g., heart and brain) and improve prognosis by inducing transient ischemia in limbs. Interestingly, the protective effect of RIC is in part attributed to the improved mitochondrial metabolism in distant ischemic organs.[14] Beyond infarcted organs, RIC treatment also shows promise in diabetes-related complications such as foot ulcers.[38] Correspondingly, the potential effect of RIC in metabolic disease is gaining interest,[39] but it remains unexplored. Here, we for the first time investigated the effects of RIC treatment in metabolic disorders, specifically testing its effect on MASH and expanding our understanding of the muscle-liver crosstalk. We observed that chronic RIC treatment alleviated liver steatosis, inflammation, and fibrogenesis in different MASH models by inducing gene expression changes toward increased fatty acid catabolism and reduced

(B and C) PCR analysis results confirmed the suppression of hepatic Nr4a3 by either miR-181d-5p overexpression (B) or RIC-conditioned mEV injection in mice (C) (n = 8 mice per group).
(D and E) WB analysis results showing NR4A3 levels in liver tissues (n = 5–6 mice per group).
(F) Luciferase activities in hepatocytes transfected with either a luciferase reporter construct containing wild-type 3′ UTR of Nr4a3 or a mutant 3′ UTR. The cells were co-transfected with miR-181d-5p mimics or control mimics. n = 5 independent experiments.
(G) Nr4a3 mRNA levels in livers from CDAHFD-fed MASH models or NC-fed control mice (n = 8 mice per group).
(H) Schematic illustration showing the study protocol.
(I–L) Comparison of liver weight/body weight ratios, hepatic triglyceride contents, and serum levels of ALT and AST between indicated groups (n = 10 mice per group).
(M) Representative H&E, Sirius red, and oil red O staining images of liver sections in indicated groups. Scale bar represents 50 μm.
(N–P) Quantitative analysis of fibrotic areas in the liver, steatosis scores, and inflammation scores in indicated groups (n = 10 mice per group).
(Q) Images of flow cytometry and quantitative analysis of monocyte and neutrophil numbers in liver tissues in indicated groups (n = 10 mice per group).
(R and S) Expression of inflammatory genes (R) and fibrotic markers (S) in liver tissues in indicated groups (n = 8 mice per group).
(T) Expression of genes involved in lipid catabolism in indicated groups (n = 8 mice per group).
(U) WB analysis results showing phosphorylation levels of S6K, S6, and JNK in indicated groups (n = 5–6 mice per group). Statistical analysis was performed by Student's t test or Mann-Whitney U test. $^{*}p < 0.05$, $^{**}p < 0.01$, $^{***}p < 0.001$. Abbreviations: AAV-ctr, intravenous injection of control AAVs; AAV-miR, intravenous injection of AAVs encoding miR-181d-5p; ALT, alanine aminotransferase; AST, aspartate aminotransferase; BW, body weight; CDAHFD, choline-deficient, L-amino acid-defined, high-fat diet; MASH, metabolic dysfunction-associated steatohepatitis; NC, normal chow; RIC, remote limb ischemic conditioning; TG, triglyceride.

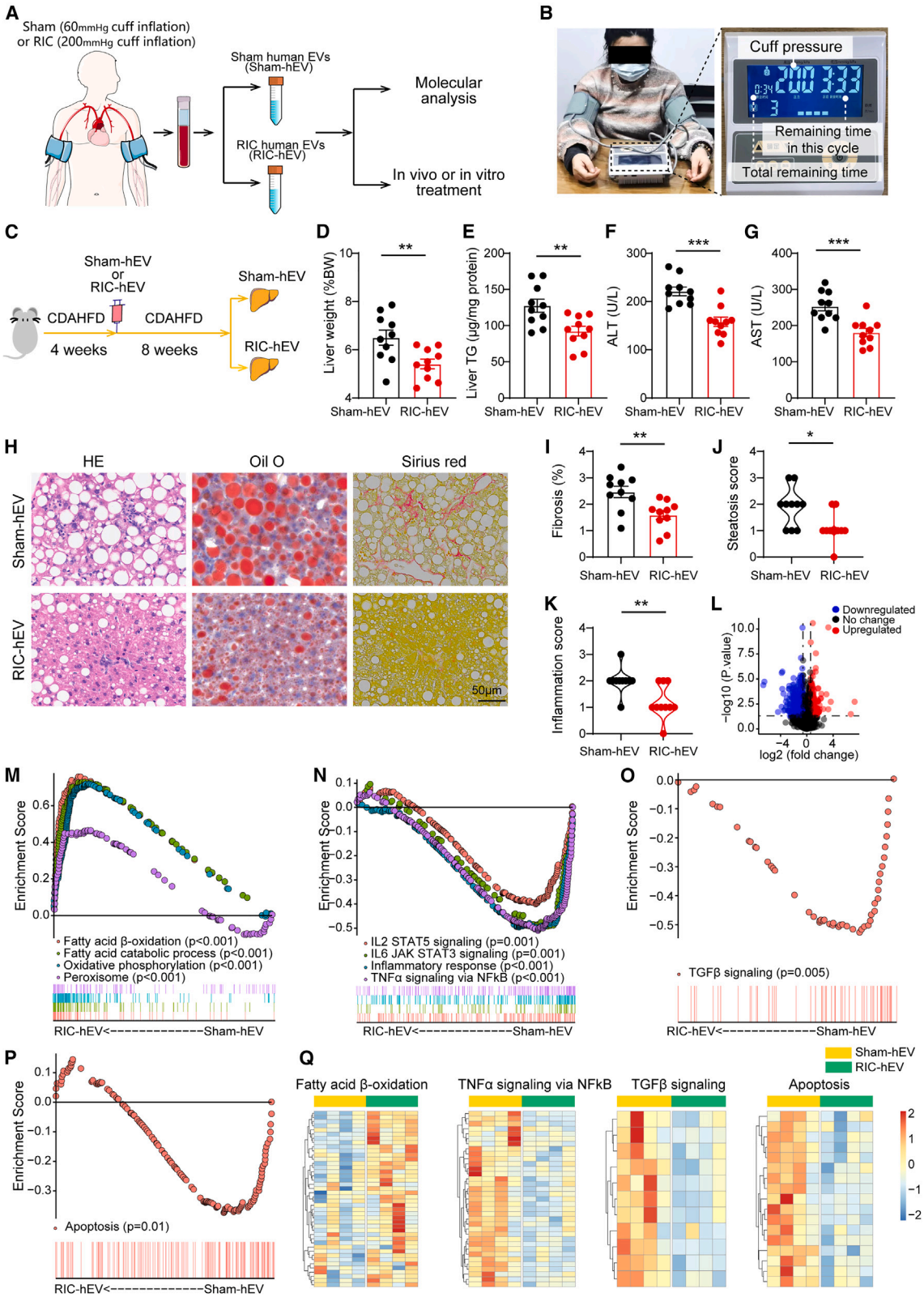

(legend on next page)

immune activation and fibrogenesis in the liver. Similar to our findings, transient ischemia in the kidney improved energy metabolism in distant tissues such as myocardium.[40] It merits further investigation whether common mechanisms underlie these metabolic benefits in remote tissues induced by transient ischemia in different organs. Together, we provided the first evidence supporting the therapeutic effects of RIC treatment in MASH, and its rapid translation into clinical trials may be expected, given that RIC can be noninvasively performed in human.

EVs, a heterogeneous population of membrane-enclosed circulating particles, play a crucial role as pivotal interorgan messengers.[21] The liver not only serves as a source of EV release but also acts as a primary recipient of EVs from various organs.[22] EVs have been identified as key regulators in MAFLD pathogenesis by facilitating communication between the liver and distant organs like adipose tissue.[5] Growing evidence indicates that skeletal muscle has the capability to release EVs into circulation, which exert biological effects in distant recipient tissues.[41] Moreover, a preferential enrichment of muscle-secreted EVs in the liver was evidenced by *in vivo* tracking.[22,23] However, the functional roles of muscle-derived EVs in the liver remain largely unknown. In this study, we demonstrated that mEVs mediated the anti-MASH effects of chronic RIC treatment. sEVs from RIC-treated muscles effectively attenuated MASH phenotypes, while blockade of muscle sEV release abolished the protective effects of RIC treatment. sEVs act as carriers of interorgan signals by encapsulating functional cargos, including proteins, metabolites, and nucleic acids.[25] Most sEV functions have been attributed to miRNAs, a class of single-stranded non-coding short RNAs.[25] Here, we demonstrated a crucial role of sEV-loaded miRNAs in mediating RIC-exerted benefits. Interestingly, among the increased miRNAs in RIC-stimulated sEVs, miR-29c-3p was reported to contribute to RIC-induced protection against hepatic ischemic injury.[42] However, despite its upregulation in sEVs, miR-29c-3p was not elevated in fatty liver tissues from RIC-treated mice, discounting a mediating role of this miRNA in RIC-induced protection against MASH. Our further screening identified miR-181d-5p as a key functional mediator of RIC-stimulated sEVs. Interestingly, miR-181d-5p is reported to be highly expressed in brain, lung, and muscle tissues, while lower levels are detected in the liver at baseline.[43] After chronic RIC treatment, we observed an upregulation of miR-181d-5p in fatty liver tissues. Moreover, hepatic miR-181d-5p overexpression suppressed hepatic lipid accumulation, inflammation, and fibrosis in MASH models and closely mirrored the transcriptomic benefits induced by RIC treatment. Aligned with current findings, multiple lines of evidence highlighted potential favorable roles of miR-181d-5p in metabolic anomalies and inflammatory disorders, including lupus nephritis, Sjögren's syndrome, and obesity.[44–46] Collectively, current findings suggest that sEV-loaded miR-181d-5p contributes to the anti-MASH effects of RIC treatment, and targeted overexpression of miR-181d-5p in liver holds therapeutic potential for MASH treatment.

MiRNAs primarily function via suppressing downstream targets.[25] Consistent with this functional mechanism, we observed that hepatic miR-181d-5p overexpression led to a suppressive pattern of global gene expression in liver (i.e., a large proportion of DEGs are downregulated). By integrating RNA-seq data with target gene prediction algorithms, we identified the transcription factor NR4A3 as a downstream target of miR-181d-5p in the current model. NR4A3 is a member of the nuclear receptor superfamily and is widely studied in cardiometabolic disease. Across cardiovascular disorders such as atherosclerosis, myocardial infarction, and cardiac hypertrophy, NR4A3 consistently claims deleterious roles by exaggerating inflammation, reactive oxidative stress, and apoptosis.[30–32] By contrast, the roles of NR4A3 in metabolic regulation remain divergent. While some studies indicated essential roles of NR4A3 in fuel utilization,[47] adipocyte-specific overexpression of NR4A3 impaired glucose tolerance,[48] and mitochondrial networks were disrupted by NR4A3 in beta-cells from pancreatic islets.[49,50] However, the role of NR4A3 in MASH is unknown. We demonstrated that NR4A3 was repressed by EV-loaded miR-181d-5p, and hepatocyte-specific NR4A3 depletion improved MASH phenotypes by leveraging immune response and lipid metabolism. While the divergent roles of the NR4A3 in metabolic regulation warrant further clarification, they reflect the cell- or tissue-specific functions of nuclear receptors. Similarly, activation of the nuclear receptor farnesoid X receptor (FXR) in the liver negatively regulates liver steatosis,[51] while intestinal FXR played an opposite role.[52] In summary, our findings elucidate the miR-181d-5p/NR4A3 axis as a molecular mechanism underlying the beneficial effects of RIC treatment in MASH and provide novel insights into signaling interconnections between muscle and liver.

In conclusion, our findings suggest that chronic RIC treatment may represent a highly translatable therapy for MASH management. This proposition is substantiated by the well-established feasibility of RIC treatment in human subjects, coupled with the

Figure 7. Administration of circulating sEVs from human volunteers undergoing RIC treatment improves MASH phenotypes induced by a CDAHFD

(A) Illustration showing collection of human circulating small EVs (hEV).

(B) Picture showing a volunteer undergoing RIC treatment.

(C) The mouse study protocol.

(D–G) Comparison of liver weight/body weight ratios, hepatic triglyceride contents, and serum levels of ALT and AST between indicated groups (n = 10 mice per group).

(H) Representative H&E, Sirius red, and oil red O staining images of liver sections in indicated groups. Scale bar represents 50 μm.

(I–K) Quantitative analysis of fibrotic areas in the liver, steatosis scores, and inflammation scores in indicated groups (n = 10 mice per group).

(L) Volcano plot of the RNA-seq analysis on liver tissues showing DEGs (n = 4 mice per group).

(M–P) GSEA results using the entire RNA-seq dataset.

(Q) Heatmap plots showing the relative gene expression enriched in indicated pathways between the two groups (n = 4 mice per group). Statistical analysis was performed by Student's t test or Mann-Whitney U test. $^{*}p < 0.05$, $^{**}p < 0.01$, $^{***}p < 0.001$. Abbreviations: ALT, alanine aminotransferase; AST, aspartate aminotransferase; BW, body weight; CDAHFD, choline-deficient, L-amino acid-defined, high-fat diet; GSEA, gene set enrichment analysis; MASH, metabolic dysfunction-associated steatohepatitis; RIC, remote limb ischemic conditioning; TG, triglyceride.

cost-effectiveness and portability of the RIC apparatus. Moreover, the identification of a novel miR-181d-5p/Nr4a3 signaling pathway mediating the anti-MASH effects of RIC treatment provides new insights into mechanisms underpinning muscle-liver crosstalk and offers valuable guidance for the future design of pharmaceutical strategies targeting MASH. Finally, this study marks the first demonstration of the direct effects of RIC treatment in a metabolic disease. These novel findings will provide rationale for and inspire future studies investigating the effects of RIC treatment in a broader spectrum of metabolic disorders.

Limitations of the study

Due to the lack of previous studies concerning the therapeutic efficacy of RIC treatment in MASH, this "proof-of-concept" study has several limitations. First, though our data obtained from mice and healthy human volunteers suggested promising benefits of RIC treatment in MASH, it remains an open question whether these findings are translatable to patients with MASH. This necessitates dedicated clinical trials, which are foreseeable soon owing to the clinically validated safety and availability of RIC treatment. Second, this study used young mice for all the experiments. It remains important to investigate whether the therapeutic effects of RIC treatment in MASH persist in elderly mice, given the significant physiological and pathological differences between young and elderly mice.[53] Third, muscle tissues experience transient hypoxia during RIC treatment. Since hypoxia induces insulin resistance in various tissues, including the liver and adipose tissue,[54,55] there may be concerns that chronic RIC could negatively impact glucose metabolism in muscle. However, unlike other tissues, acute hypoxia induced by exercise or direct anoxic conditions has been shown to increase glucose uptake in muscle,[56] suggesting a low likelihood of this risk. Nonetheless, further investigation is warranted to fully understand the effects of chronic RIC on muscle glucose metabolism.

RESOURCE AVAILABILITY

Lead contact

Further information and requests for resources and reagents should be directed to and will be fulfilled by the lead contact, Jun Pu (pujun310@hotmail.com).

Materials availability

Further requests for materials should be directed to and will be fulfilled by the lead contact.

Data and code availability

- RNA-seq and miRNA-seq data have been deposited at GEO and are publicly available. The accession number is listed in the key resources table.
- This paper does not report the original code.
- Unprocessed data in this manuscript are available as Data S1.
- The datasets generated in this study are available from the lead contact.

ACKNOWLEDGMENTS

This work was supported by the Noncommunicable Chronic Diseases-National Science and Technology Major Project (2023ZD0503204), the National Natural Science Foundation of China (82421001, 82270342, 82230014, 82071731, 82471732, and 82192864), the Innovative Research Team of High-Level Local Universities in Shanghai (SHSMU-ZDCX20210700), the Science and Technology Commission of Shanghai Municipality (22QA1405400), the Shanghai Municipal Health Commission (20234Y0048, QNWS2024109, SHWSRS(2023)-62, 2022JC013, and 2023ZZ02021), and the Postdoctoral Fellowship Program of CPSF (GZC20231637).

AUTHOR CONTRIBUTIONS

J.P. and Y.Z. designed the experiments and oversaw all aspects of study conduct and manuscript preparation. Y.Z., Ling Gao, J.C., J.W., W.W., W.H., and K.H. performed the experiments. Lingchen Gao and G.L. analyzed the data. W.Z. and A.Y. contributed reagents, materials, and analysis tools. Y.Z. and Ling Gao wrote the paper. J.P., K.Q., and A.F.C. edited the paper.

DECLARATION OF INTERESTS

The authors declare no competing interests.

STAR★METHODS

Detailed methods are provided in the online version of this paper and include the following:

- KEY RESOURCES TABLE
- EXPERIMENTAL MODEL AND STUDY PARTICIPANT DETAILS
  - Mice
  - Primary mouse and human hepatocytes
  - Human subjects
- METHOD DETAILS
  - Establishment of MASH models
  - RIC treatment in mice
  - Establishment of parabiosis models
  - AAV-mediated gene manipulation
  - Extracellular vesicle isolation and treatment
  - Micro-PET/CT scanning
  - Biochemical analysis
  - Insulin and glucose tolerance test
  - Histopathological analysis and scoring
  - Measurement of the hydroxyproline content
  - TUNEL assay
  - Flow cytometry and gating strategy
  - Nanoparticle tracking analysis and TEM
  - Western blot analysis
  - Polymerase chain reaction
  - RNA-seq library preparation and sequencing
  - MicroRNA sequencing and analysis
  - Primary hepatocyte culture and treatment
  - Assays in primary hepatocytes
  - Fatty acid oxidation (FAO) assay
  - Luciferase assay
- QUANTIFICATION AND STATISTICAL ANALYSIS

SUPPLEMENTAL INFORMATION

Supplemental information can be found online at https://doi.org/10.1016/j.cmet.2025.02.009.

Received: February 15, 2024
Revised: August 30, 2024
Accepted: February 25, 2025
Published: March 20, 2025

REFERENCES

1. Riazi, K., Azhari, H., Charette, J.H., Underwood, F.E., King, J.A., Afshar, E.E., Swain, M.G., Congly, S.E., Kaplan, G.G., and Shaheen, A.A. (2022). The prevalence and incidence of NAFLD worldwide: a systematic review and meta-analysis. Lancet Gastroenterol. Hepatol. *7*, 851–861.
2. Geier, A., Tiniakos, D., Denk, H., and Trauner, M. (2021). From the origin of NASH to the future of metabolic fatty liver disease. Gut *70*, 1570–1579.

3. Noureddin, M., Vipani, A., Bresee, C., Todo, T., Kim, I.K., Alkhouri, N., Setiawan, V.W., Tran, T., Ayoub, W.S., Lu, S.C., et al. (2018). NASH Leading Cause of Liver Transplant in Women: Updated Analysis of Indications for Liver Transplant and Ethnic and Gender Variances. Am. J. Gastroenterol. *113*, 1649–1659.
4. Shroff, H., and VanWagner, L.B. (2020). Cardiovascular Disease in Nonalcoholic Steatohepatitis: Screening and Management. Curr. Hepatol. Rep. *19*, 315–326.
5. Azzu, V., Vacca, M., Virtue, S., Allison, M., and Vidal-Puig, A. (2020). Adipose Tissue-Liver Cross Talk in the Control of Whole-Body Metabolism: Implications in Nonalcoholic Fatty Liver Disease. Gastroenterology *158*, 1899–1912.
6. Kuang, J., Wang, J., Li, Y., Li, M., Zhao, M., Ge, K., Zheng, D., Cheung, K.C.P., Liao, B., Wang, S., et al. (2023). Hyodeoxycholic acid alleviates non-alcoholic fatty liver disease through modulating the gut-liver axis. Cell Metab. *35*, 1752–1766.e8.
7. Thyfault, J.P., and Rector, R.S. (2020). Exercise Combats Hepatic Steatosis: Potential Mechanisms and Clinical Implications. Diabetes *69*, 517–524.
8. Zhaoxin, Z., Jianying, S., Yan, Z., Jianren, W., Yujing, S., Weijing, L., and Yawei, X. (2023). Research Progress in Heart Rate Variability Applications in Exercise Rehabilitation for Cardiovascular Diseases. CVIA *8*.
9. Carlson, S.A., Fulton, J.E., Schoenborn, C.A., and Loustalot, F. (2010). Trend and prevalence estimates based on the 2008 Physical Activity Guidelines for Americans. Am. J. Prev. Med. *39*, 305–313.
10. Justine, M., Azizan, A., Hassan, V., Salleh, Z., and Manaf, H. (2013). Barriers to participation in physical activity and exercise among middle-aged and elderly individuals. Singapore Med. J. *54*, 581–586.
11. Jean-St-Michel, E., Manlhiot, C., Li, J., Tropak, M., Michelsen, M.M., Schmidt, M.R., McCrindle, B.W., Wells, G.D., and Redington, A.N. (2011). Remote preconditioning improves maximal performance in highly trained athletes. Med. Sci. Sports Exer. *43*, 1280–1286.
12. Geng, X., Wang, Q., Lee, H., Huber, C., Wills, M., Elkin, K., Li, F., Ji, X., and Ding, Y. (2021). Remote Ischemic Postconditioning vs. Physical Exercise After Stroke: an Alternative Rehabilitation Strategy? Mol. Neurobiol. *58*, 3141–3157.
13. Chen, H.S., Cui, Y., Li, X.Q., Wang, X.H., Ma, Y.T., Zhao, Y., Han, J., Deng, C.Q., Hong, M., Bao, Y., et al. (2022). Effect of Remote Ischemic Conditioning vs Usual Care on Neurologic Function in Patients With Acute Moderate Ischemic Stroke: The RICAMIS Randomized Clinical Trial. JAMA *328*, 627–636.
14. Kleinbongard, P., Gedik, N., Kirca, M., Stoian, L., Frey, U., Zandi, A., Thielmann, M., Jakob, H., Peters, J., Kamler, M., et al. (2018). Mitochondrial and Contractile Function of Human Right Atrial Tissue in Response to Remote Ischemic Conditioning. J. Am. Heart Assoc. *7*, e009540.
15. Matsumoto, M., Hada, N., Sakamaki, Y., Uno, A., Shiga, T., Tanaka, C., Ito, T., Katsume, A., and Sudoh, M. (2013). An improved mouse model that rapidly develops fibrosis in non-alcoholic steatohepatitis. Int. J. Exp. Pathol. *94*, 93–103.
16. Huang, W., Pang, Y., Liu, Q., Liang, C., An, S., Wu, Q., Zhang, Y., Huang, G., Chen, H., Liu, J., et al. (2023). Development and Characterization of Novel FAP-Targeted Theranostic Pairs: A Bench-to-Bedside Study. Research (Wash D. C) *6*, 0282.
17. Mori, Y., Dendl, K., Cardinale, J., Kratochwil, C., Giesel, F.L., and Haberkorn, U. (2023). FAPI PET: Fibroblast Activation Protein Inhibitor Use in Oncologic and Nononcologic Disease. Radiology *306*, e220749.
18. Lonardo, A., Nascimbeni, F., Ballestri, S., Fairweather, D., Win, S., Than, T.A., Abdelmalek, M.F., and Suzuki, A. (2019). Sex Differences in Nonalcoholic Fatty Liver Disease: State of the Art and Identification of Research Gaps. Hepatology *70*, 1457–1469.
19. Zhang, X.J., Ji, Y.X., Cheng, X., Cheng, Y., Yang, H., Wang, J., Zhao, L.P., Huang, Y.P., Sun, D., Xiang, H., et al. (2021). A small molecule targeting ALOX12-ACC1 ameliorates nonalcoholic steatohepatitis in mice and macaques. Sci. Transl. Med. *13*, eabg8116.
20. Gao, L., Zhao, Y., Wu, H., Lin, X., Guo, F., Li, J., Long, Y., Zhou, B., She, J., Zhang, C., et al. (2023). Polycystic Ovary Syndrome Fuels Cardiovascular Inflammation and Aggravates Ischemic Cardiac Injury. Circulation *148*, 1958–1973.
21. Wang, J., Li, L., Zhang, Z., Zhang, X., Zhu, Y., Zhang, C., and Bi, Y. (2022). Extracellular vesicles mediate the communication of adipose tissue with brain and promote cognitive impairment associated with insulin resistance. Cell Metab. *34*, 1264–1279.e8.
22. Whitham, M., Parker, B.L., Friedrichsen, M., Hingst, J.R., Hjorth, M., Hughes, W.E., Egan, C.L., Cron, L., Watt, K.I., Kuchel, R.P., et al. (2018). Extracellular Vesicles Provide a Means for Tissue Crosstalk during Exercise. Cell Metab. *27*, 237–251.e4.
23. Estrada, A.L., Valenti, Z.J., Hehn, G., Amorese, A.J., Williams, N.S., Balestrieri, N.P., Deighan, C., Allen, C.P., Spangenburg, E.E., Kruh-Garcia, N.A., et al. (2022). Extracellular vesicle secretion is tissue-dependent ex vivo and skeletal muscle myofiber extracellular vesicles reach the circulation in vivo. Am. J. Physiol. Cell Physiol. *322*, C246–C259.
24. Ostrowski, M., Carmo, N.B., Krumeich, S., Fanget, I., Raposo, G., Savina, A., Moita, C.F., Schauer, K., Hume, A.N., Freitas, R.P., et al. (2010). Rab27a and Rab27b control different steps of the exosome secretion pathway. sup pp 1; sup pp 1-13. Nat. Cell Biol. *12*, 19–30.
25. Isaac, R., Reis, F.C.G., Ying, W., and Olefsky, J.M. (2021). Exosomes as mediators of intercellular crosstalk in metabolism. Cell Metab. *33*, 1744–1762.
26. Chendrimada, T.P., Gregory, R.I., Kumaraswamy, E., Norman, J., Cooch, N., Nishikura, K., and Shiekhattar, R. (2005). TRBP recruits the Dicer complex to Ago2 for microRNA processing and gene silencing. Nature *436*, 740–744.
27. McGeary, S.E., Lin, K.S., Shi, C.Y., Pham, T.M., Bisaria, N., Kelley, G.M., and Bartel, D.P. (2019). The biochemical basis of microRNA targeting efficacy. Science *366*, eaav1741.
28. Chen, Y., and Wang, X. (2020). miRDB: an online database for prediction of functional microRNA targets. Nucleic Acids Res. *48*, D127–D131.
29. Pfister, D., Núñez, N.G., Pinyol, R., Govaere, O., Pinter, M., Szydlowska, M., Gupta, R., Qiu, M., Deczkowska, A., Weiner, A., et al. (2021). NASH limits anti-tumour surveillance in immunotherapy-treated HCC. Nature *592*, 450–456.
30. Cheng, Z., Völkers, M., Din, S., Avitabile, D., Khan, M., Gude, N., Mohsin, S., Bo, T., Truffa, S., Alvarez, R., et al. (2011). Mitochondrial translocation of Nur77 mediates cardiomyocyte apoptosis. Eur. Heart J. *32*, 2179–2188.
31. Feng, X.J., Gao, H., Gao, S., Li, Z., Li, H., Lu, J., Wang, J.J., Huang, X.Y., Liu, M., Zou, J., et al. (2015). The orphan receptor NOR1 participates in isoprenaline-induced cardiac hypertrophy by regulating PARP-1. Br. J. Pharmacol. *172*, 2852–2863.
32. Zhao, Y., Howatt, D.A., Gizard, F., Nomiyama, T., Findeisen, H.M., Heywood, E.B., Jones, K.L., Conneely, O.M., Daugherty, A., and Bruemmer, D. (2010). Deficiency of the NR4A orphan nuclear receptor NOR1 decreases monocyte adhesion and atherosclerosis. Circ. Res. *107*, 501–511.
33. Fang, Z., Kim, H.G., Huang, M., Chowdhury, K., Li, M.O., Liangpunsakul, S., and Dong, X.C. (2021). Sestrin Proteins Protect Against Lipotoxicity-Induced Oxidative Stress in the Liver via Suppression of C-Jun N-Terminal Kinases. Cell. Mol. Gastroenterol. Hepatol. *12*, 921–942.
34. Vicencio, J.M., Yellon, D.M., Sivaraman, V., Das, D., Boi-Doku, C., Arjun, S., Zheng, Y., Riquelme, J.A., Kearney, J., Sharma, V., et al. (2015). Plasma exosomes protect the myocardium from ischemia-reperfusion injury. J. Am. Coll. Cardiol. *65*, 1525–1536.
35. Wang, H., Maimaitiaili, R., Yao, J., Xie, Y., Qiang, S., Hu, F., Li, X., Shi, C., Jia, P., Yang, H., et al. (2021). Percutaneous Intracoronary Delivery of Plasma Extracellular Vesicles Protects the Myocardium Against Ischemia-Reperfusion Injury in Canis. Hypertension *78*, 1541–1554.

36. Musso, G., Cassader, M., Cohney, S., Pinach, S., Saba, F., and Gambino, R. (2015). Emerging Liver-Kidney Interactions in Nonalcoholic Fatty Liver Disease. Trends Mol. Med. *21*, 645–662.

37. Chakravarthy, M.V., Siddiqui, M.S., Forsgren, M.F., and Sanyal, A.J. (2020). Harnessing Muscle-Liver Crosstalk to Treat Nonalcoholic Steatohepatitis. Front. Endocrinol. *11*, 592373.

38. Regulski, M., Greenwood, T., and Leschinsky, B. (2021). Impact of repeated remote ischemic conditioning on diabetic foot ulcers: A proof-of-concept study. Wound Repair Regen. *29*, 853–858.

39. Liu, J., Sun, X., Jin, H., Yan, X.L., Huang, S., Guo, Z.N., and Yang, Y. (2021). Remote ischemic conditioning: A potential therapeutic strategy of type 2 diabetes. Med. Hypotheses *146*, 110409.

40. Takaoka, A., Nakae, I., Mitsunami, K., Yabe, T., Morikawa, S., Inubushi, T., and Kinoshita, M. (1999). Renal ischemia/reperfusion remotely improves myocardial energy metabolism during myocardial ischemia via adenosine receptors in rabbits: effects of "remote preconditioning". J. Am. Coll. Cardiol. *33*, 556–564.

41. Ma, S., Xing, X., Huang, H., Gao, X., Xu, X., Yang, J., Liao, C., Zhang, X., Liu, J., Tian, W., et al. (2023). Skeletal muscle-derived extracellular vesicles transport glycolytic enzymes to mediate muscle-to-bone crosstalk. Cell Metab. *35*, 2028–2043.e7.

42. Duan, Y.F., Sun, D.L., Chen, J., Zhu, F., and An, Y. (2017). MicroRNA-29a/b/c targets iNOS and is involved in protective remote ischemic preconditioning in an ischemia-reperfusion rat model of non-alcoholic fatty liver disease. Oncol. Lett. *13*, 1775–1782.

43. Zhang, Y., Li, C., Guan, C., Zhou, B., Wang, L., Yang, C., Zhen, L., Dai, J., Zhao, L., Jiang, W., et al. (2020). MiR-181d-5p Targets KLF6 to Improve Ischemia/Reperfusion-Induced AKI Through Effects on Renal Function, Apoptosis, and Inflammation. Front. Physiol. *11*, 510.

44. Abu-Farha, M., Cherian, P., Al-Khairi, I., Nizam, R., Alkandari, A., Arefanian, H., Tuomilehto, J., Al-Mulla, F., and Abubaker, J. (2019). Reduced miR-181d level in obesity and its role in lipid metabolism via regulation of ANGPTL3. Sci. Rep. *9*, 11866.

45. Chai, F., Peng, H., Qin, L., Liu, C., Zeng, Y., Wang, R., Xu, G., Wang, R., Wei, G., Huang, H., et al. (2024). MicroRNA miR-181d-5p regulates the MAPK signaling pathway by targeting mitogen-activated protein kinase 8 (MAPK8) to improve lupus nephritis. Gene *893*, 147961.

46. Castro, I., Carvajal, P., Jara, D., Aguilera, S., Heathcote, B., Barrera, M.J., Aliaga-Tobar, V., Maracaja-Coutinho, V., Urzúa, U., Quest, A.F.G., et al. (2022). Small RNA Expression Profiling Reveals hsa-miR-181d-5p Downregulation Associated With TNF-α Overexpression in Sjögren's Syndrome Patients. Front. Immunol. *13*, 870094.

47. Fu, Y., Luo, L., Luo, N., Zhu, X., and Garvey, W.T. (2007). NR4A orphan nuclear receptors modulate insulin action and the glucose transport system: potential role in insulin resistance. J. Biol. Chem. *282*, 31525–31533.

48. Walton, R.G., Zhu, X., Tian, L., Heywood, E.B., Liu, J., Hill, H.S., Liu, J., Bruemmer, D., Yang, Q., Fu, Y., et al. (2016). AP2-NR4A3 transgenic mice display reduced serum epinephrine because of increased catecholamine catabolism in adipose tissue. Am. J. Physiol. Endocrinol. Metab. *311*, E69–E81.

49. Close, A.F., Dadheech, N., Villela, B.S., Rouillard, C., and Buteau, J. (2019). The orphan nuclear receptor Nor1/Nr4a3 is a negative regulator of β-cell mass. J. Biol. Chem. *294*, 4889–4897.

50. Close, A.F., Dadheech, N., Lemieux, H., Wang, Q., and Buteau, J. (2020). Disruption of Beta-Cell Mitochondrial Networks by the Orphan Nuclear Receptor Nor1/Nr4a3. Cells *9*, 168.

51. Clifford, B.L., Sedgeman, L.R., Williams, K.J., Morand, P., Cheng, A., Jarrett, K.E., Chan, A.P., Brearley-Sholto, M.C., Wahlström, A., Ashby, J.W., et al. (2021). FXR activation protects against NAFLD via bile-acid-dependent reductions in lipid absorption. Cell Metab. *33*, 1671–1684.e4.

52. Jiang, C., Xie, C., Li, F., Zhang, L., Nichols, R.G., Krausz, K.W., Cai, J., Qi, Y., Fang, Z.Z., Takahashi, S., et al. (2015). Intestinal farnesoid X receptor signaling promotes nonalcoholic fatty liver disease. J. Clin. Invest. *125*, 386–402.

53. Pálovics, R., Keller, A., Schaum, N., Tan, W., Fehlmann, T., Borja, M., Kern, F., Bonanno, L., Calcuttawala, K., Webber, J., et al. (2022). Molecular hallmarks of heterochronic parabiosis at single-cell resolution. Nature *603*, 309–314.

54. Gu, C.J., Yi, H.H., Feng, J., Zhang, Z.G., Zhou, J., Zhou, L.N., Zhou, J.P., Li, M., and Li, Q.Y. (2018). Intermittent Hypoxia Disrupts Glucose Homeostasis in Liver Cells in an Insulin-Dependent and Independent Manner. Cell. Physiol. Biochem. *47*, 1042–1050.

55. Regazzetti, C., Peraldi, P., Grémeaux, T., Najem-Lendom, R., Ben-Sahra, I., Cormont, M., Bost, F., Le Marchand-Brustel, Y., Tanti, J.F., and Giorgetti-Peraldi, S. (2009). Hypoxia decreases insulin signaling pathways in adipocytes. Diabetes *58*, 95–103.

56. Soo, J., Raman, A., Lawler, N.G., Goods, P.S.R., Deldicque, L., Girard, O., and Fairchild, T.J. (2023). The role of exercise and hypoxia on glucose transport and regulation. Eur. J. Appl. Physiol. *123*, 1147–1165.

57. Liang, W., Menke, A.L., Driessen, A., Koek, G.H., Lindeman, J.H., Stoop, R., Havekes, L.M., Kleemann, R., and van den Hoek, A.M. (2014). Establishment of a general NAFLD scoring system for rodent models and comparison to human liver pathology. PLoS One *9*, e115922.

58. Gan, L., Xie, D., Liu, J., Bond Lau, W., Christopher, T.A., Lopez, B., Zhang, L., Gao, E., Koch, W., Ma, X.L., et al. (2020). Small Extracellular Microvesicles Mediated Pathological Communications Between Dysfunctional Adipocytes and Cardiomyocytes as a Novel Mechanism Exacerbating Ischemia/Reperfusion Injury in Diabetic Mice. Circulation *141*, 968–983.

59. Wang, Y.F., Li, R.H., Tong, R.Y., Chen, T.W., Sun, M.Z., Luo, L.J., Li, Z., Chen, Y.F., Zhao, Y.C., Zhang, C.S., et al. (2025). Integrating single-cell RNA and T cell/B cell receptor sequencing with mass cytometry reveals dynamic trajectories of human peripheral immune cells from birth to old age. Nat. Immunol. *26*, 308–322.

60. Zhao, Y., Lu, X., Wan, F., Gao, L., Lin, N., He, J., Wei, L., Dong, J., Qin, Z., Zhong, F., et al. (2022). Disruption of Circadian Rhythms by Shift Work Exacerbates Reperfusion Injury in Myocardial Infarction. J. Am. Coll. Cardiol. *79*, 2097–2115.

STAR★METHODS

KEY RESOURCES TABLE

REAGENT or RESOURCE	SOURCE	IDENTIFIER
Antibodies		
Rabbit polyclonal anti-CD63	Abcam	Cat#ab216130;RRID:AB_3076642
Rabbit polyclonal anti-Calnexin	Abcam	Cat#ab22595; RRID:AB_2069006
Rabbit monoclonal anti-Dicer	Abcam	ab259327
Rabbit polyclonal anti-NOR1/NR4A3	Abcam	Cat#ab94507; RRID:AB_10861336
Mouse monoclonal anti-TSG101	Abcam	Cat#ab83; RRID:AB_306450
Mouse monoclonal anti-beta-Actin	Abcam	Abcam Cat#ab8224; RRID:AB_449644
Rabbit polyclonal anti-CD9	Zen BioScience	Cat#380441; RRID:AB_2941746
Rabbit monoclonal anti-GM130	Zen BioScience	Cat# R380777; RRID:AB_3099513
Rabbit polyclonal anti-p70 S6K	Cell Signaling Technology	Cat#9202; RRID:AB_331676
Rabbit monoclonal anti-phospho-S6K	Cell Signaling Technology	Cat#9234; RRID:AB_2269803
Mouse monoclonal anti-S6	Cell Signaling Technology	Cat#2317; RRID:AB_2238583
Rabbit monoclonal anti-phospho-S6	Cell Signaling Technology	Cat#5364; RRID: AB_10694233
Rabbit monoclonal anti-phospho-JNK	Proteintech	Cat#80024-1-RR; RRID:AB_2882943
Rabbit monoclonal anti-JNK	Beyotime	Cat#AF1048; RRID:AB_2923148
Rat Monoclonal anti-mouse CD45-PE/Cyanine7	Biolegend	Cat#103114, clone 30-F11; RRID:AB_312979
Rat Monoclonal anti-mouse CD11b-APC	Biolegend	Cat#101212, clone M1/70; RRID:AB_312795
Rat monoclonal anti-mouse F4/80-PE	Biolegend	Cat#123110, clone BM8; RRID:AB_893486
Rat monoclonal anti-mouse Ly-6G-Brilliant Violet 421™	Biolegend	Cat#127627, clone 1A8; RRID:AB_10897944
Rat monoclonal anti-mouse Ly-6G-Brilliant Violet 711™	Biolegend	Cat#127643, clone 1A8; RRID:AB_2565971
Rat monoclonal anti-mouse CD115-Brilliant Violet 421™	Biolegend	Cat#135513, clone AFS98; RRID:AB_2562667
Rat monoclonal anti-mouse Ly-6C-PerCP/Cyanine5.5	Biolegend	Cat#128011, clone HK1.4; RRID:AB_1659242
Bacterial and virus strains		
AAV-MHCK7-mir30-m-shRNA(Dicer)	This paper	N/A
AAV-MHCK7-scramble	This paper	N/A
AAV-TBG-miR-181d-5p	This paper	N/A
AAV-TBG-scramble	This paper	N/A
AAV-sponge (miR-181d-5p)	This paper	N/A
AAV-scramble	This paper	N/A
AAV-MHCK7-Cre	This paper	N/A
AAV-MHCK7	This paper	N/A
AAV-TBG-Nr4a3/EGFP	This paper	N/A
Biological samples		
Plasma from humans	This paper	N/A
Plasma from mice	This paper	N/A
Liver tissue from mice	This paper	N/A
Muscle tissue from mice	This paper	N/A
Chemicals, peptides, and recombinant proteins		
Collagenase IV	Worthington	LS004188; CAS: 9001-12-1
Palmitate acid	Sigma-Aldrich	P0500; CAS: 57-10-3
Zombie UV™ Fixable Viability Kit	Biolegend	Cat# 423107

(*Continued on next page*)

Continued

REAGENT or RESOURCE	SOURCE	IDENTIFIER
[^{68}Ga]Ga-DOTA-FAPI	This paper	N/A
Exosome Green Fluorescent Labeling Dye (PKH67)	Umibio	Cat#UR52303
Exosome Fluorescent Dye (DiR)	Umibio	Cat#UR21017
Oil red O	Sangon	A600395; CAS : 1320-06-5
Mitochondrial membrane potential assay kit	Beyotime	Cat#C2003S
Critical commercial assays		
Triglyceride Content Enzymatic Assay Kit	Applygen	Cat#E1013
In Situ Cell Death Detection Kit	Roche	REF#11684795910
Hydroxyproline (HYP) Colorimetric Assay Kit	Elabscience	Cat#E-BC-K062-M
NEBNext Small RNA Library Prep Set for Illumina	NEB	Cat#NEB#E7330S
exoRNeasy Serum/Plasma Starter Kit	Qiagen	Cat#77023
VAHTS Universal RNA-seq Library Prep Kit	Vazyme	Cat#NR604-01/02
TruSeq Stranded mRNA LTSample Prep Kit	Illumina	Cat#20020594
Dual Luciferase Reporter Assay System	Promega	E1910
Lactate Dehydrogenase (LDH) Assay Kit	Promega	G1780
Seahorse Palmitate stress kit	Agilent	Cat#103693
Deposited data		
Raw and analyzed data	This paper	GEO: GSE255528
Experimental models: Cell lines		
Mouse primary hepatocytes	This paper	N/A
Human primary hepatocytes	Liver Biotech	N/A
Experimental models: Organisms/strains		
Mouse: Rab27a$^{f/f}$ and Rab27a^{cKO}	Gempharmatech	N/A
Mouse: NR4A3$^{f/f}$ and NR4A3^{cKO}	Gempharmatech	N/A
Mouse: Hepatic miR-181d-5p-OE C57BL/6J mice	This paper	N/A
Mouse: Hepatic miR-181d-5p-inhibiting C57BL/6J mice	This paper	N/A
Mouse: C57BL/6J mice	Gempharmatech	N/A
Oligonucleotides		
Primers for qPCR, see Supplemental Table S2	This paper	N/A
mmu-miR-669a-3p mimic-Sense	This paper	ACAUAACAUACACACACACGUAU
mmu-miR-669a-3p mimic-Antisense	This paper	ACGUGUGUGUGUAUGUUAUGUUU
mmu-miR-181d-5p mimic-Sense	This paper	AACAUUCAUUGUUGUCGGUGGGU
mmu-miR-181d-5p mimic-Antisense	This paper	CCACCGACAACAAUGAAUGUUUU
mmu-miR-466a-3p mimic-Sense	This paper	UAUACAUACACGCACACAUAAGA
mmu-miR-466a-3p mimic-Antisense	This paper	UUAUGUGUGCGUGUAUGUAUAUU
mimics NC-Sense	This paper	UUGUACUACACAAAAGUACUG
mimics NC-Antisense	This paper	GUACUUUUGUGUAGUACAAUU
Recombinant DNA		
WT Nr4a3 3'-UTR reporter plasmid	QianMo Biotechnology	N/A
Mutant Nr4a3 3'-UTR reporter plasmid	QianMo Biotechnology	N/A
Software and algorithms		
The R Project	The R Foundation	https://www.r-project.org/
Microsoft 365	Microsoft	https://www.microsoft.com/zh-cn/microsoft-365/buy/compare-all-microsoft-365-products?tab=1

(*Continued on next page*)

Continued

REAGENT or RESOURCE	SOURCE	IDENTIFIER
Other		
RIC apparatus	GTHR Medical Technology	L300A
CDAHFD diet	Shuyu Biotechnology	N/A
HFHC diet	TrophicDiet	Cat#TP26304
Centrifugal Filter Unit	Millipore	Cat#UFC910024
qEVoriginal Columns	IZON	https://store.izon.com/collections/qev/products/qevoriginal?variant=42763128307884
Nanoparticle Tracking Analysis system	Malvern panalytical	Nanosight NS300
Small Animal Fluorescence & Bioluminescence Imaging System	Vieworks	InVivo Smart-LF
Cellular Energy Metabolism Analysis System	Agilent	Seahorse XFe96

EXPERIMENTAL MODEL AND STUDY PARTICIPANT DETAILS

Mice

All animal studies were approved by the Institutional Animal Ethics Committee at Renji Hospital, School of Medicine, Shanghai Jiao Tong University. C57BL/6 mice, C57BL/6J-*Rab27a*^{em1Cflox} (*Rab27a*$^{fl/fl}$), C57BL/6J-*Nr4a3*^{em1Cflox} (*Nr4a3*$^{fl/fl}$), C57BL/6J$^{em1Cin(Alb-iCre)}$ (Alb-Cre) were purchased from GemPharmatech (Nanjing, China). *Nr4a3*$^{fl/fl}$ mice were crossed with Alb-cre mice to obtain liver-specific *Nr4a3* knockout mice, and *Rab27a*$^{fl/fl}$ mice were injected with AAV-MHCK7-Cre to obtain muscle-specific *Rab27a* knockout mice. Male and female mice, aged 8 to 10-week-old, were used in this study. All animals were housed in a specific-pathogen-free facility at 24°C±2°C, humidity of 40%±5%, under a constant 12-hour light/12-hour dark cycle. Chow and water were available *ad libitum*.

Primary mouse and human hepatocytes

The primary mouse hepatocytes were isolated through a digestion-based method. Briefly, 8-week-old C57BL/6J mice were anesthetized with isoflurane and the portal vein and vena cava were exposed. The inferior vena cava was cannulated and perfused with perfusion buffer, followed by perfusion with collagenase IV digestion solution (0.5mg/ml). After adequate digestion, the liver was removed, torn apart, and triturated in a 10-cm dish containing digestion medium. The suspension was passed through a 70-μm cell strainer and centrifuged at 50g for 2 minutes. After three washes, the hepatocytes were resuspended in DMEM medium and checked for viability with trypan blue staining. The cells were plated and cultured at 37°C containing 5% CO2 in the air. The primary human hepatocytes were provided by Liver biotech (Shenzhen, China), and cultured at 37°C containing 5% CO2 with culture medium (LV-WEM001).

Human subjects

The human protocol was approved by the Ethics Committee of Renji Hospital, School of Medicine, Shanghai Jiao Tong University. We recruited 20 human volunteers to test the therapeutic efficacy of circulating EVs from human volunteers undergoing RIC treatment in steatotic primary human hepatocytes and mouse models of MASH. Informed consent was signed for all participants. Participants aged over 18 years were included. Exclusion criteria included the following: (1) intolerance to RIC treatment; (2) a history of vascular thrombosis in upper limbs; (3) current or planning pregnancy; (4) refractory hypertension (defined as systolic blood pressure > 180 mmHg and/or diastolic blood pressure > 110 mmHg after medical treatment); (5) experiencing acute disorders of any origins; (6) malignant tumor. Participants were assigned to either RIC or sham treatment for 4 weeks. For RIC and sham treatment, an automatic RIC device (GTHR Medical Technology, Shenzhen, China) was used. Both upper limbs were simultaneously subjected to four cycles of cuff inflation at 200 mmHg (5 minutes for each cycle) and cuff relaxation (5 minutes for each cycle). This procedure was performed once daily. Sham treatment was performed in the same way except that the cuff pressure was set to 60 mmHg during inflation.

METHOD DETAILS

Establishment of MASH models

We used two mouse models of MASH in current study. (1) To establish the CDAHFD-induced MASH model, the mice were fed a L-amino-defined high fat (45% kcal), choline deficient diet with 0.1% methionine (CDAHFD, Shuyu Biotechnology) for a total of 12 weeks. (2) To establish the HFHC-induced MASH model, the mice were fed an HFHC diet consisting of 14% protein, 42% fat, and 44% carbohydrates and containing 0.2% cholesterol (TrophicDiet) for a total of 18 weeks. Mice that were fed an NC diet consisting of 20.6% protein, 12.0% fat, and 67.4% carbohydrates (kilocalories) (TrophicDiet) served as normal controls.

RIC treatment in mice

The RIC treatment was performed in four cycles, each consisting of 5-minute hindlimb occlusion followed by 5-minute reperfusion (35 minutes in total). Specifically, mice were anesthetized with isoflurane (2% in oxygen), and tourniquets were gently tightened on the bilateral hindlimbs to block blood flow. Hindlimb occlusion and reperfusion were monitored by a laser doppler perfusion imaging system (PeriCam PSI System; Perimed, Järfälla, Sweden). Sham operation was performed as described above, but the tourniquets were not fastened.

Establishment of parabiosis models

To test whether RIC treatment protects against MASH via circulating factors, parabiosis models were established. Briefly, the corresponding lateral aspects of each donor and recipient mouse were shaved, and matching skin incisions were made from behind the ear to the tail. For easier suturing, the subcutaneous fascia was bluntly dissected. The elbow and knee joints were joined using a 5-0 silk suture. Afterwards, the dorsal and ventral skin flaps were joined using continuous sutures. A subcutaneous injection of buprenorphine (0.1mg/kg in saline) was administered immediately after the procedure and repeated every 6 hours for 72 hours. The parabiotic pairs may have difficulties in food uptake at beginning and were fed moist mash diet for 1 week.

AAV-mediated gene manipulation

To silence Dicer expression in the hindlimb muscle, mice were anesthetized and AAV vectors encoding shRNA targeting Dicer (1.0×10^{12} genome copies) were injected into each of the bilateral hindlimbs using a Hamilton syringe with a 31G needle. Ten sites per hindlimb were administrated. For control mice, control AAV vectors were injected in the same way. To assess the impact of miR-181d-5p overexpression on MASH, 8-week-old mice were intravenously injected with either control AAV8 vectors or AAV8 encoding miR-181d-5p (1.0×10^{12} genome copies). To antagonize endogenous miR-181d-5p, mice were intravenously injected with either control AAV8 vectors or AAV8 encoding miR-181d-5p sponge (1.0×10^{12} genome copies).

Extracellular vesicle isolation and treatment

To isolate extracellular vesicles from human or mouse plasma, plasma was diluted in phosphate buffered saline, centrifuged at 3,000g for 15 min to remove debris, followed by centrifugation at 10,000g for 30 min. The supernatant was then centrifuged at 110,000g for 70 min. The pelleted extracellular vesicles were resuspended in PBS and used for further study. To collect EV-free plasma, plasma samples were centrifuged at 110,000g overnight, and supernatants were collected. The isolation of sEVs from skeletal muscle was performed with a slight modification of previously reported method.[23] Specifically, hindlimb muscles distal to the tourniquet were collected from RIC- or sham-treated mice. The muscle tissues were cut into approximately 0.5 cm^3 pieces and rinsed gently in sterile PBS. These segments were cultured in suspension culture bottles with EVs-free media at 37°C under 5% CO_2. At 48 hours after incubation, the culture media was filtered through 100 μm cell strainers. The media was then centrifuged at 3,000g for 15 min to remove tissue debris, followed by centrifugation at 10,000g for 30 min. Then, the supernatants were concentrated with ultrafiltration (Amicon Ultra-15, Milipore), and sEVs were isolated using qEV columns (Izon Science) based on size exclusion chromatography. Protein content was measured using a BCA protein assay kit (Thermo Scientific). The *in vitro* sEV treatment was detailed in the "Primary hepatocyte culture and treatment" section. For sEV treatment in mice, sEVs harvested from the skeletal muscles of RIC- or sham-treated mice were intravenously injected for 8 weeks (1×10^{10} particles/once weekly).

Micro-PET/CT scanning

Mice were anesthetized and intravenously injected with [^{68}Ga]Ga-DOTA-FAPI. Images were acquired using an IRIS PET/CT system (Inviscan Imaging Systems). The PET images were reconstructed using a 3-Dimensional Ordered Subsets Expectation Maximum (OSEM3D) algorithm, followed by Maximization/Maximum a Posteriori (MAP) or FastMAP. The data were processed with OsiriX Lite software (Pixmeo SARL) and Inveon Research Workplace (Siemens Preclinical Solutions). The regions of interest (ROIs) were drawn over the liver according to CT images. The tracer uptake was measured using the Inveon Research Workplace software 3.0, and the individual quantification of [^{68}Ga]Ga-DOTA-FAPI uptake was calculated for each mouse. The mean standardized uptake values (SUV) were determined by dividing the relevant ROI intensity by the ratio of the injected activity to the body weight.

Biochemical analysis

Plasma ALT, AST, total cholesterol (TC), triglyceride (TG), high density lipoprotein cholesterol (HDL-c), and low density lipoprotein cholesterol (LDL-c) were measured with an automated biochemical analyzer (Rayto Chemray 240, Shenzhen, China). For measurement of hepatic TG contents, commercial kits were used according to the manufacturer's instructions (Applygen Technologies Inc., Beijing, China).

Insulin and glucose tolerance test

Animals were fasted (12-hour food withdrawal) overnight for GTT or fasted for 2 hours for ITT. Glucose (2g/kg body weight, for GTT) or insulin (0.5 U/kg body weight, for ITT) was injected intraperitoneally. Blood was collected from the tail vein and glucose levels were measured at 0 min (prior to glucose or insulin administration) and different time points afterwards (30/60/90/120 min for GTT, 15/30/60/90 min for ITT).

Histopathological analysis and scoring

The livers were removed, and the same lobe of each liver was fixed in 4% paraformaldehyde, embedded in paraffin or optimum cutting temperature (OCT)-freeze medium, and sectioned for staining. The paraffin sections were stained with H&E staining and Sirius red staining, and the OCT sections were stained with oil-red staining. Images were acquired using a light microscope (Leica, Germany), and steatosis and inflammation scores were determined using a recognized scoring system for rodent MAFLD models.[57] Specifically, steatosis was scored based on the percentage of the total area affected into the following categories: 0 (<5%), 1 (5–33%), 2 (34–66%) and 3 (>66%). Inflammation was evaluated by counting the number of inflammatory foci per field at 100× magnification. An inflammatory focus was defined a cluster of $\geq$5 inflammatory cells. Five different fields were counted and the average was scored into the following categories: 0 (<0.5 foci), 1 (0.5–1.0 foci), 2 (1.0–2.0 foci), 3 (>2.0 foci).

Measurement of the hydroxyproline content

The hepatic hydroxyproline contents were determined by a Hydroxyproline Assay Kit according to the manufacturer's instructions (E-BC-K062-M, Elabscience). Frozen liver tissues (100 mg) were acid-hydrolyzed with 1 mL HCl (6mol/L) at 95 °C for 6 h. After centrifugation and sequential addition of working solutions per protocol, the supernatant was used for the colorimetric assay.

TUNEL assay

Hepatocyte apoptosis in the livers was determined by terminal deoxynucleotidyl transferase dUTP nick-end labeling (TUNEL) staining via an In Situ Cell Death Detection Kit (Roche Diagnostics). Hepatocytes were labeled by anti-albumin (Alb) antibody (Proteintech, 16475-1-AP), apoptotic nuclei were identified by green fluorescein staining, and total nuclei were stained by 4',6-diamidino-2-phenylindole (DAPI). Apoptotic index was expressed as the percentage of TUNEL-positive hepatocyte number over total hepatocyte number.

Flow cytometry and gating strategy

Cell suspension preparation. Peripheral blood was collected and red blood cells were lysed in RBC lysis buffer (Beyotime). Mice were perfused with 30 mL of ice-cold PBS to remove residual blood, followed by collection of liver, spleen, and bones. The livers were weighed, cut into small pieces in a 6-well plate and digested with 3 mL of collagenase IV digestion solution (0.5mg/ml) at 37°C for 60 min. The digested liver was dissociated and passed through a 70μm cell strainer, and were collected by centrifugation. Splenocytes were obtained by crushing the spleen through a 40μm cell strainer and flushed with PBS. Splenocytes were centrifuged, and red blood cells were lysed. Bone marrow cells were collected by flushing bones with PBS, and cell solutions were passed through a 40μm cell strainer. All the cells were washed with PBS and live/dead cells were stained with Zombie UV™ Fixable Viability Kit (Biolegend). To block nonspecific binding of antibodies to Fcγ receptors, cell suspensions were first incubated with anti-CD16/32 antibody (biolegend) at 4°C for 5 min before incubation with mixed antibodies. The following antibodies were used for flow cytometric analysis: anti-mouse CD45-PE/Cyanine7 (103114, clone 30-F11), anti-mouse CD11b-APC (101212, clone M1/70), anti-mouse F4/80-PE (123110, clone BM8), anti-mouse Ly-6G-Brilliant Violet 421™ (127627, clone 1A8), anti-mouse Ly-6G-Brilliant Violet 711™ (127643, clone 1A8), anti-mouse CD115-Brilliant Violet 421™ (135513, clone AFS98), anti-mouse Ly-6C-PerCP/Cyanine5.5 (128011, clone HK1.4). All antibodies were from Biolegend. Absolute cell counts were calculated by adding Precision Count Beads™ (424902, Biolegend) in samples. In the liver, cells were identified as monocytes ($Live^+CD45^+CD11b^+Ly\text{-}6G^-Ly\text{-}6C^{High}$) and neutrophils ($Live^+CD45^+CD11b^+Ly\text{-}6G^+Ly\text{-}6C^{Low}$). In peripheral blood, spleen, and bone marrow, cells were identified as monocytes ($Live^+CD45^+CD11b^+CD115^+$), $Ly\text{-}6C^{hi}$ monocytes ($Live^+CD45^+CD11b^+Ly\text{-}6G^-CD115^+F4/80^-Ly\text{-}6C^{high}$), and neutrophils ($Live^+CD45^+CD11b^+CD115^-Ly\text{-}6G^+$).

Nanoparticle tracking analysis and TEM

EVs were first resuspended in PBS and diluted for further analysis. NTA was performed using a NanoSight NS300 system (Malvern panalytical). For electron microscopy, ten microliters of EVs were loaded on a TEM grid, fixed with a filtered 3% uranyl acetate solution, followed by removal of uranyl acetate solution from the grid by contacting the grid's edge with filter paper. Then, samples were observed in a transmission electron microscope (Hitachi).

Western blot analysis

Proteins were extracted by lysis, and the total proteins were subjected to sodium dodecyl sulphate–polyacrylamide gel electrophoresis (SDS-PAGE), with gel concentrations determined based on the molecular weight of the target proteins. The gels were transferred onto nitrocellulose membranes, and incubated with specific primary antibodies overnight at 4°C: CD63 (1:1000; ab216130), Calnexin (1:1000; ab22595), Dicer (1:1000; ab259327), NR4A3 (1:1000; ab94507), TSG101 (1:1000; ab83), and beta-Actin (1:1000; ab8224) from Abcam; CD9 (380441; 1:1000), and GM130 (1:1000; R380777) from Zen BioScience; S6K (1:1000; #9202), phospho-S6K (1:1000; #9234), S6 (1:1000; #2317), phospho-S6 (1:1000; #5364) from Cell Signaling Technology; phospho-JNK (1:1000; 80024-1-RR) from Proteintech; JNK (1:1000; AF1048) from Beyotime. After incubation with the corresponding secondary antibodies, the protein bands were visualized using enhanced chemiluminescence.

Polymerase chain reaction

Total RNA was isolated using TRIzol or an exoRNeasy Serum/Plasma Starter Kit (Qiagen). For detection of mRNA levels, total RNA was applied to cDNA synthesis using a RT Kit (Vazyme Biotech Co.,Ltd, Nanjing, China). The mRNA expression was measured by

quantitative PCR with a Premix Kit (Vazyme Biotech Co., Ltd, Nanjing, China) in a LightCycler® 480 Real-time PCR System (Roche Applied Science). Beta-actin was used as an internal control, and the primer information is presented in Table S2. For miRNA detection, total RNA was subjected to reverse transcription using the miDETECT A TrackTM miRNA qRT-PCR Starter Kit (RiboBio Co., Ltd, Guangzhou, China). Quantitative RT-PCR was performed using miDETECT A Track^{TM} miRNA qPCR Primers (RiboBio Co.,Ltd, Guangzhou, China) according to the manufacturer's instructions. U6 RNA was used as a reference control for cells and tissues. To compare the levels of target miRNAs within EVs, the cel-miR-39 miRNA (QianMo Biotechnology, Shanghai, China) was added as a spike-in control.[58] Results were calculated and expressed as fold change relative to the indicated control groups.

RNA-seq library preparation and sequencing

The RNA-sequencing raw data are available in Gene Expression Omnibus (GEO:GSE255524, GEO:GSE255526, and GEO:GSE255527). Liver tissues were collected, and total RNA was extracted. Briefly, RNA integrity was evaluated using the Agilent 2100 Bioanalyzer (Agilent Technologies, Santa Clara, CA, USA). The samples with RNA Integrity Number (RIN) $\geq$ 7 were subjected to the subsequent analysis.[59,60] The libraries were constructed using VAHTS Universal RNA-seq Library Prep Kit for Illumina (Vazyme Biotech) or TruSeq Stranded mRNA LTSample Prep Kit (Illumina) according to the manufacturer's instructions. Then these libraries were sequenced on the Illumina HiSeq X Ten platform or Illumina NovaSeq 6000 and paired-end reads were generated.

Raw reads were processed using Trimmomatic. Clean reads were aligned against the mouse genome (GRCm38) using hisat2, and the read counts of genes were obtained by htseq-count. Gene expression changes were identified using the DESeq package. Differentially expressed genes (DEGs) were defined as the genes with nominal p-values < 0.05 and an absolute value of fold change > 1.5. To explore the pathway and biological changes induced by RIC treatment, gene set enrichment analysis (GSEA) was performed using the entire gene expression datasets, and normalized enrichment score for each gene set was calculated. Gene ontology (GO) and Kyoto Encyclopedia of Genes and Genomes (KEGG) enrichment analysis of DEGs were respectively performed based on the hypergeometric distribution.

MicroRNA sequencing and analysis

The miRNA-sequencing raw data are available in Gene Expression Omnibus (GEO:GSE255525). EV-containing RNAs were extracted using exoRNeasy Serum/Plasma Starter Kit (Qiagen, 77023). NEBNext Small RNA Library Prep Set for Illumina Kits for the small RNA library construction (Cat. No. NEB#E7330S, NEB, USA) following the manufacturer's recommendations. The libraries were finally sequenced using the Illumina Novaseq 6000 platform. The small RNA sequencing was conducted in OE Biotech Co., Ltd. (Shanghai, China). The basic reads were converted into sequence data by base calling. Low quality reads were filtered, and the reads with 5' primer contaminants and poly (A) were removed. The reads without 3' adapter and insert tag, the reads shorter than 15 nt or longer than 41 nt from the raw data were filtered, and the clean reads were obtained. Known miRNAs were identified by aligning against miRBase v22 database (http://www.mirbase.org/). Based on the hairpin structure of a pre-miRNA and the miRBase database, the corresponding miRNA star sequence and miRNA mature sequence were also identified. Differential expression analysis was performed using DESeq package. To identify target genes of miR-181d-5p, common target genes in both human and mouse species were first predicted from TargetScan and miRDB databases, and intersected with downregulated genes by miR-181d-5p.

Primary hepatocyte culture and treatment

Lipotoxicity was induced in primary mouse and human hepatocytes with palmitic acid (PA, 0.5mM) for 24 hours. Primary mouse hepatocytes were seeded in 24-well plates, and co-incubated with PA and different volumes of plasma from RIC-treated or control mice. Based on the results from total plasma treatment, EVs (5μg/ml) or EV-free plasma (10% v/v) were added in each well of 24-well plates, to explore their individual effects in PA-treated primary mouse hepatocytes. EVs isolated from human plasma (5μg/ml) were added in primary human hepatocytes in each well. To investigate the effects of muscle-derived EVs, different dosages of muscle-derived EVs (10^1, 10^2, $0.5*10^3$, 10^3 particles/cell) were added in PA-treated primary mouse hepatocytes. To screen the functional miRNAs, miRNA mimics or control mimics (10nM) were transfected in PA-treated primary mouse hepatocytes.

Assays in primary hepatocytes

Hepatocyte lactate dehydrogenase (LDH) release was measured using a Cytotox 96® non-radioactive cytotoxicity assay kit (Promega) according to the manufacturer's protocol. Briefly, following experimental treatment, 50μL hepatocyte culture supernatant was transferred to a 96-well plate and an equal volume of CytoTox 96 ® Reagent is added to each well and incubated for 30 minutes. After addition of 50μL stop solution, and the absorbance signal is measured at 490nm in a plate reader. Hepatocyte apoptosis was measured with an In Situ Cell Death Detection Kit (Roche Diagnostics). Mitochondrial membrane potential was detected using 5,5',6,6'-tetrachloro-1,1',3,3'-tetraethyl-imidacarbocyanine iodide (JC-1) staining method (Beyotime). The cellular lipid accumulation was determined by Oil Red O staining.

Fatty acid oxidation (FAO) assay

The FAO of primary hepatocytes was measured using a Seahorse XFe96 Flux Analyzer with a Palmitate Oxidation Stress Test Kit (Agilent Technologies). The cells were seeded in XF96 cell culture microplates coated with collagen type I (Gibco) and incubated with EVs or miRNA mimics for 24 hours. Then the culture medium was replaced with substrate-limited medium for 16 hours.

Subsequently, the cells were assayed following manufacturer's protocols, with addition of 1 μM oligomycin, 1.5 μM carbonyl cyanide-4-(trifluoromethoxy)phenylhydrazone (FCCP), and 1 μM each of rotenone and antimycin A.

Luciferase assay

The luciferase reporter assay was performed with a reporter plasmid carrying the 3'-untranslated regions (UTR) of Nr4a3 (WT reporter), or a mutant 3'-UTR in which the miR-181d-5p binding site was mutated (mutant reporter). Briefly, the hepatocytes were transfected with the WT or mutant reporter (QianMo Biotechnology, Shanghai, China), along with miR-181d-5p mimics or control mimic. After 48-hour transfection, the luciferase activities were assayed using the Dual Luciferase Reporter Assay System (Promega, USA).

QUANTIFICATION AND STATISTICAL ANALYSIS

Continuous variables were tested for normality using the Q-Q plot and Shapiro-Wilk test, and homogeneity of variance was tested using Levene's test. Differences in continuous data were compared using Student's *t*-test, the Mann-Whitney *U* test, paired *t*-test, or a paired permutation test when appropriate. For comparison among multiple groups, one-way analysis of variance (ANOVA) with Tukey's post-hoc test or Welch's ANOVA test with the Games-Howell post-hoc test was used. For comparisons of continuous data involving two independent variables, two-way ANOVA was performed, and data were transformed when assumptions were violated. For comparisons of ordinal data involving two independent variables, two-way ordinal regression with CLM was performed, and ART ANOVA is used when the assumptions for the regression method were violated. All statistical analyses were performed using R version 3.6.0 (R Foundation for Statistical Computing, Vienna, Austria). A p-value (two-sided) <0.05 was deemed significant.